

# Understanding crack versus cavitation in pressure-sensitive adhesives: the role of kinetics

Jérémie Teisseire, Frédéric Nallet, Pascale Fabre, Cyprien Gay  
 Centre de recherche Paul-Pascal–CNRS,

115 avenue Schweitzer, F-33600 Pessac, FRANCE

[http://www.crpp-bordeaux.cnrs.fr/ext/rubrique.php3?id\\_rubrique=8](http://www.crpp-bordeaux.cnrs.fr/ext/rubrique.php3?id_rubrique=8)

Please send reprint requests to [cgay@crpp-bordeaux.cnrs.fr](mailto:cgay@crpp-bordeaux.cnrs.fr)

February 6, 2008

## Abstract

We perform traction experiments on viscous liquids highly confined between parallel plates, a geometry known as the probe-tack test in the adhesion community. Direct observation during the experiment coupled to force measurement shows the existence of several mechanisms for releasing the stress. Bubble nucleation and instantaneous growth had been observed in a previous work. Upon increasing further the traction velocity or the viscosity, the bubble growth is progressively delayed. At high velocities, cracks at the interface between the plate and the liquid appear before the bubbles have grown to their full size. Bubbles and cracks are thus observed concomitantly. At even higher velocities, cracks develop fully so early that the bubbles are not even visible. We present a theoretical model that describes these regimes, using a Maxwell fluid as a model for the actual fluid, a highly viscous silicon oil. We present the resulting phase diagramme for the different force peak regimes. The predictions are compatible with the data. Our results show that in addition to cavitation, interfacial cracks are encountered in a probe-tack traction test with viscoelastic, *liquid* materials and not solely with viscoelastic solids like adhesives.

## 1 Introduction

Some materials display immediate stickiness, a property known as “tackiness” [1, 2]. The deformability of such materials enables them to achieve a good contact with all kinds of solid bodies, including those with surface roughness: Dahlquist’s criterion [3, 4], widely used since the mid-1960s, states that a solid material is sticky if its elastic shear modulus is lower than  $10^5$ Pa. In order to be usable as an adhesive, a deformable material should not flow on large time scales: it must be a viscoelastic *solid*.

In a classical test [5], called the probe-tack test in the adhesion community, a thin film of adhesive material is deposited on a planar, rigid surface. It is then tested with another planar, rigid surface, while the force is being recorded. The film is first compressed. After some “contact time”, it is subjected to traction. The traction force displays two characteristic features [5] before the separation is complete: a peak and a plateau. The reason for the force being relieved immediately after the peak can be traced back to two main mechanisms in usual adhesives. The most common one is cavitation, as evidenced by the first tests that included direct visualisation through the sample thickness [6]. Another, classical relief mechanism is the propagation of interfacial cracks. This occurs especially [5] when the elastic modulus of the material is high (low temperature or dense cross-linking).

Whether the cracks appear at the sample edge (“external cracks”<sup>1</sup>) or on multiple spots at the sample/indenter interface (“internal cracks”) is mainly a question of sample aspect ratio [7, 8].

<sup>1</sup>We use the names introduced by Crosby *et al.*[7]

We here concentrate on how “internal” cracks and cavitation compete and interact. To address these questions, we continue the approach we used for cavitation [9] and study cavitation and crack phenomena in model material (viscoelastic liquids) both from an experimental and from a theoretical point of view. On such liquids (silicon oils), observed failure mechanisms include cavitation [10] as well as “external” cracks from the sample edge [11] in JKR geometry.

In the present work, we first reexamine the usual cavitation and crack criteria (section 2). We then describe the protocols and materials used (section 3). We present the experimental results and observations and offer a description of the underlying mechanisms (section 4). We then construct a theoretical model to account for the triggering of the observed mechanisms (section 5) and compare its predictions with the experimental results. We finally provide some discussion on the compared rheology of silicon oils and real adhesives in the context of our experiments (section 6).

## 2 Cavitation and crack thresholds

Cavitation and crack mechanisms are commonly encountered in adhesive films under traction. In the present section, we review and discuss the threshold stress needed to trigger them in the case of a purely elastic material.

### 2.1 Cavitation and crack: an introduction

#### 2.1.1 Cavitation

Cavitation in elastomeric materials under traction has been known since the experiments and calculations by Gent *et al* in the 1960s [12]. The corresponding threshold for cavitation reflects the elastic resistance that the material opposes to the growth of inner, preexisting bubbles, and is commonly used in the context of adhesive materials [7]. For a full description of the cavitation process, one needs to consider other physical ingredients which affect the pressure required for bubble growth: the dilation of the bubble gas during bubble growth and the corresponding lower pressure, and the bubble surface tension which tends to make it shrink [13].

#### 2.1.2 Crack

Apart from cavitation, another mechanism is commonly encountered in adhesives films under traction: cracks often develop at the interface between the adhesive film and the indenter.

#### 2.1.3 Method

In the present section, we consider an elastic material that initially contains nuclei for both mechanisms: bulk microbubbles (radius  $R_0$ ) and microscopic cracks (size  $b$ ) at the interface with the indenter. We take into account the possibility of propagation of interfacial cracks as well as all three ingredients involved in cavitation (elasticity, surface tension, gas pressure), and provide a very crude formulation for the corresponding stress threshold, restricting ourselves to scaling laws.

## 2.2 Cavitation

We now examine the physical ingredients that determine the cavitation threshold, discussed by Gent and collaborators [12, 13], for an elastic material initially containing microbubbles, see Figure 1.

#### 2.2.1 Elasticity

In the regime where the cavitation threshold essentially reflects the elastic resistance of the material to bubble growth, the critical stress was calculated by Gent *et al* in the 1960s [13]. In the case of

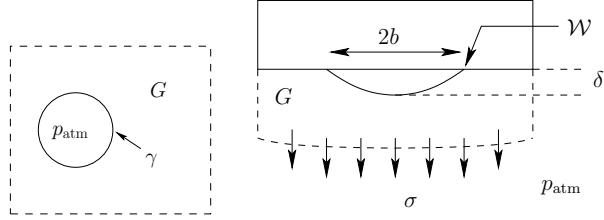


Figure 1: Left: bulk cavitation. Three main physical ingredients resist cavity growth and determine the (non-homogeneous) cavitation pressure threshold in an elastic medium: gas dilation (contribution on the order of the atmospheric pressure), cavity surface tension  $\gamma$  and elasticity (modulus  $G$ ) of the medium that surrounds the cavity.

Figure 2: Right: interfacial crack. Main physical ingredients that determine crack propagation at the interface between a solid body and a deformable elastic material: applied stress  $\sigma$ , elastic modulus  $G$ , local separation energy  $\mathcal{W}$  for propagation (equation 7), atmospheric pressure  $p_{\text{atm}}$ . The dimensions  $b$  and  $\delta$  of the crack are also indicated.

a neo-Hookean material, it is on the order of the (shear) elastic modulus:

$$\sigma_{\text{Gent}} \simeq G \quad (1)$$

### 2.2.2 Dilation

The growth of a microbubble to millimetric size implies a strong dilation of the enclosed gas. The bubble growth rate is usually by far too fast for any gas diffusion from the bulk towards the growing bubble to develop significantly. As a result, the pressure in the growing bubble drops by an amount that is on the order of the atmospheric pressure. This contributes towards the cavitation threshold stress. When this term is dominant, the threshold is therefore:

$$\sigma_{\text{dilation}} \simeq p_{\text{atm}} \quad (2)$$

### 2.2.3 Surface tension

The surface tension at the bubble interface also contributes towards the cavitation threshold stress. When this term is dominant, the threshold therefore reflects the Laplace tensile stress exerted by the bubble interface on the elastic sample outside the bubble. It is proportional to surface tension and to the curvature of the bubble surface:

$$\sigma_{\text{Laplace}} \simeq \frac{\gamma}{R_0} \quad (3)$$

### 2.2.4 Cavitation threshold

All three above ingredients enter the cavitation threshold for an elastic material initially containing microbubbles. A rough, simplified expression for the threshold is obtained as the sum (or the maximum) of all three values:

$$\begin{aligned} \sigma_{\text{cavitation}} &\simeq p_{\text{atm}} + G + \frac{\gamma}{R_0} \\ &\simeq \max \left\{ p_{\text{atm}}; G; \frac{\gamma}{R_0} \right\} \end{aligned} \quad (4)$$

The value of these thresholds is reported on figure 3.

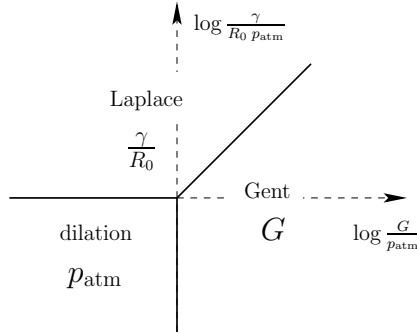


Figure 3: Gent-Tompkins diagramme for the stress threshold values for a bulk spherical cavity (log-log plot). The effective threshold is the largest of the three values given by elastic deformation ( $G$ ), gas dilation ( $p_{\text{atm}}$ ) and Laplace pressure ( $\gamma/R_0$ ).

## 2.3 Interfacial crack propagation

Let us now assume that disk-shaped cracks of size  $b$  are present at the interface between the (elastic) adhesive material and the (undeformable) indenter (see figure 2). We are interested in the value of the tensile stress that is required to induce the propagation of such *internal* cracks<sup>2</sup>.

### 2.3.1 Thermodynamic work

The thermodynamic energy  $\mathcal{W}_0$  involved in opening such a crack includes the surface tension of the destroyed (adhesive/indenter) interface as well as those of both newly created (adhesive/air and indenter/air) interfaces:

$$\mathcal{W}_0 = \gamma_{\text{adh}} + \gamma_{\text{ind}} - \gamma_{\text{ind-adh}} \quad (5)$$

This Dupré energy is the simplest version of the work needed to separate both surfaces on the molecular scale.

In practice, the energy needed locally to detach the adhesive from the solid substrate is larger than  $\mathcal{W}_0$ . More elaborate estimations include local dissipation mechanisms such as the role of polymer molecules at or near the interface [14, 15]:

$$\mathcal{W} > \mathcal{W}_0 \quad (6)$$

In general, the interfacial energy cost corresponding to the crack of size  $b$  can thus be estimated as

$$\mathcal{W} b^2 \quad (7)$$

### 2.3.2 Griffith's crack propagation criterion

When a uniform, normal, tensile stress  $\sigma$  is exerted onto the elastic material, the presence of the interfacial crack induces a slight reduction of the elastic energy since the crack essentially cannot transmit stress but is able to provide some extra volume to neighbouring regions. If the crack width  $b$  is increased, the interfacial cost (equation 7) is enhanced while the elastic energy is further reduced. For a high enough value of the applied stress  $\sigma$ , increasing the crack width  $b$  reduces the elastic energy to a greater extent than it increases the interfacial energy. As a result, the crack propagates under such a high applied tensile stress.

This condition for crack propagation [16] is known as Griffith's criterion for crack. Omitting numerical prefactors of order unity, it can be written as:

$$\sigma_{\text{Griffith}} \simeq \sqrt{G \mathcal{W}/b} \quad (8)$$

<sup>2</sup>We use the names introduced by Crosby *et al.*[7]: *internal* cracks are located at the adhesive/indenter interface, while *external* cracks propagate from the edge of the adhesive/indenter contact region.

### 2.3.3 Crack and dilation

Griffith's approach was introduced in the context of hard, hardly deformable materials. In such a context, the crack thickness  $\delta$  (see Figure 2) is still very small at the onset of propagation, and the crack volume is thus always very small prior to propagation. For softer materials such as adhesives, the crack volume may increase sufficiently for the work done against atmospheric pressure to become predominant over the (Griffith) elastic and interfacial work. The propagation threshold is then on the order of  $p_{\text{atm}}$ . As a result, the crack threshold can be reformulated as:

$$\begin{aligned}\sigma_{\text{surf}} &\simeq p_{\text{atm}} + \sqrt{\frac{WG}{b}} \\ &\simeq \max \left\{ p_{\text{atm}}; \sqrt{\frac{WG}{b}} \right\}\end{aligned}\quad (9)$$

Expression (9), where all numerical factors have been omitted, extends equation (8) to softer materials or weaker interface strengths, which may be relevant in some cases for adhesives.<sup>3</sup> The asymptotic regimes of this expression are presented schematically on Figure 4.

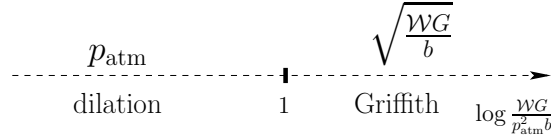


Figure 4: Stress threshold values for a thin, interfacial crack. The effective threshold (expression 9) is the largest of Griffith's value  $\sqrt{GW/b}$  and of atmospheric pressure  $p_{\text{atm}}$ .

We now compare the above expression for the interfacial crack threshold and the bulk cavitation threshold (4). These thresholds will be central in our understanding of the experiments presented in sections 3 and 4.

## 2.4 Competition between crack and cavitation

Let us now determine how interfacial failure and bulk cavitation compete in the case of a purely elastic material. Since both the interfacial cracks of initial size  $b$  and the bulk cavities of initial size  $R_0$  (see Figures 1 and 2) are subjected to the same applied stress  $\sigma$ , the failure with the lower threshold will trigger first<sup>4</sup>.

### 2.4.1 General expression for the threshold

Comparing expressions (4) and (9), we can therefore approximate the global failure threshold as:

$$\begin{aligned}\sigma &\simeq \min [\sigma_{\text{bulk}}; \sigma_{\text{surf}}] \\ &\simeq \min \left[ \max \left\{ p_{\text{atm}}; G; \frac{\gamma}{R_0} \right\}; \right. \\ &\quad \left. \max \left\{ p_{\text{atm}}; \sqrt{\frac{WG}{b}} \right\} \right]\end{aligned}\quad (10)$$

<sup>3</sup>Expression (9) is not always valid, however, as its derivation assumes that the shape of the crack remains disk-like. In other words, until propagation occurs, the crack thickness  $\delta$  must remain smaller than its width  $b$ . Also, the role of the trapped air [17], which partly relieves the pressure difference with the outside air, is not taken into account. A more elaborate discussion will be presented separately.

<sup>4</sup>The initially triggered failure mechanism may not be predominant eventually, as discussed later in this article.

### 2.4.2 On the size of bulk microbubbles

In view of Figure 3, the initial size  $R_0$  of bulk microbubbles is sometimes important to determine the cavitation threshold.

In practice, in order to form small microbubbles (such that  $\gamma/R_0 > p_{\text{atm}}$ ), one needs to incorporate small amounts of gas in the material during the formulation process. In order to achieve that, one needs to apply high enough stresses to overcome the corresponding Laplace pressure, *i.e.*, stresses in excess of  $10^5$  Pa.

In the following, for the sake of simplicity, we shall assume that this is *not* the case, *i.e.*, that only larger bubbles are present ( $\gamma/R_0 < p_{\text{atm}}$ ). Hence, the dilation contribution dominates over the surface tension contribution.

As a result, the  $\gamma/R_0$  term in expression (10) can be left out, and the general expression for the threshold can be simplified as:

$$\sigma \simeq \min \left[ \max \{p_{\text{atm}}; G\}; \max \left\{ p_{\text{atm}}; \sqrt{\frac{\mathcal{W}G}{b}} \right\} \right] \quad (11)$$

### 2.4.3 Large bulk microbubbles and strong interface

Let us now consider an elastic sample with large bulk microbubbles (such that  $\gamma/R_0 < p_{\text{atm}}$ ). Equation (11) is then especially interesting for a strong interface ( $\mathcal{W} > bp_{\text{atm}}$ ), as represented on Figure 5.

- For very soft materials, both the cavitation threshold and the crack threshold are close to  $p_{\text{atm}}$ . It is therefore impossible to determine simply which mechanism will occur (bulk cavitation or surface crack). It probably depends mainly on the local disorder in the material ( $G$ ) or in the interface ( $\mathcal{W}$  or  $b$ ).
- When the elastic modulus is increased (between letters A and B on Figure 5), the surface threshold (Griffith regime) becomes larger than the bulk threshold (at atmospheric pressure), and bulk cavitation is triggered first.
- When the elastic modulus is further increased (between B and C), the bulk threshold remains lower than the crack threshold even though it now increases (Gent's regime), thus cavitation is still triggered first.
- For large values of the elastic modulus (on the right-hand side of letter C), the cavitation threshold becomes larger than the crack threshold: surface cracks are then triggered first.

## 2.5 Dahlquist criterion and Gent's cavitation threshold

Dahlquist's criterion [4] for an elastic material to display adhesive properties states that its elastic modulus should be lower than around  $10^5$  Pa.

In view of the above discussion, given that this numerical value corresponds to atmospheric pressure, it appears that Dahlquist's criterion coincides with the crossover between two regimes for cavitation in an elastic material: Gent's elastic regime ( $\sigma_{\text{seuil}} = G$ ) and the dilation regime ( $\sigma_{\text{seuil}} = p_{\text{atm}}$ ).

$$G \simeq p_{\text{atm}}, \quad (12)$$

In practice, since the elastic modulus of many pressure-sensitive adhesives is lower than  $p_{\text{atm}}$ , Gent's cavitation threshold may not be fully relevant for soft adhesives. Instead, we expect the dilation and Laplace cavitation thresholds as well Griffith's threshold for crack to be predominant in such materials.

More precisely, if microbubbles are not too small (paragraph 2.4.2) and if the interface is strong, one expects the failure threshold for soft adhesives ( $G < p_{\text{atm}}$ ) to be always governed by dilation (atmospheric threshold, corresponding to the left-hand side of point B on Figure 5). We

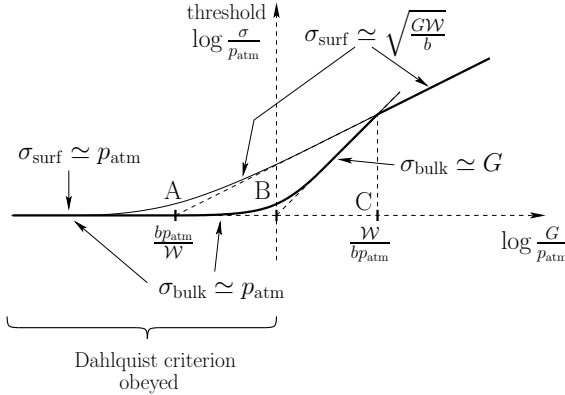


Figure 5: Stress threshold values as a function of the elastic modulus  $G$  (log-log plot) when bulk microbubbles are not too small ( $\gamma/R_0 > p_{\text{atm}}$ ) and when the interface is strong ( $\mathcal{W}/(bp_{\text{atm}}) > 1$ ). The overall stress threshold (thick line) results from the competition between bulk and surface thresholds. Hard materials (on the right-hand side of letter C) undergo interfacial separation (Griffith's criterion  $\sqrt{GW/b}$ ). Moderately hard materials (between B and C) obey Gent's cavitation threshold  $G$  related to elasticity. Soft materials (on the left of B), which obey Dahlquist's criterion (*i.e.*,  $G < p_{\text{atm}}$ ), all have an atmospheric stress threshold due to dilation. Moderately soft materials (between A and B) cavitate in the bulk, while very soft materials ( $G \ll p_{\text{atm}}^2 b/\mathcal{W}$ , some distance on the left of letter A) exhibit either bulk cavitation or surface crack, depending on local material disorder.

also expect the failure mechanism to be cavitation for moderately soft materials (between points A and B on Figure 5), and either cavitation or crack for very soft materials (left-hand side of point A).

### 3 Protocol, materials and experiments

#### 3.1 Apparatus

The general geometry for a probe-tack test is the following: it consists in two horizontal and parallel plates whose separation  $h$  can be varied. One of the two plates is mounted onto a carriage (location  $l$ ) *via* a load cell. The material is initially deposited onto the fixed plate. The moving plate is slowly approached, for instance until the material is confined into a film of prescribed thickness  $h_0$ . The material is then allowed to relax for a prescribed duration  $t_c$ , known as the contact time. The carriage is eventually pulled at a constant nominal velocity  $V \equiv \dot{l}$  while the force  $F$  is being recorded.

Two different traction machines are used for the experimental part of the present work. The first one is a commercial equipment (Z2.5/TN1S, Zwick Roell, Germany), the second one is a home-made prototype. The nominal separation velocity can be varied by about four orders of magnitude, from typically  $1 \mu\text{m/s}$  to  $10 \text{ mm/s}$ . We usually mount load cells with a  $100 \text{ N}$ -capacity, but other transducers with a lesser capacity (for instance,  $10 \text{ N}$ ) can also be used, if necessary. Both machines yield time  $t$ , force  $F$  and carriage location  $l$  as digital data with an acquisition rate fixed at  $50 \text{ Hz}$  (commercial machine), or adjustable up to  $1000 \text{ Hz}$  (home-made prototype).

A piece of polished, optical glass (BFI Optilas, France) is used as the fixed plate with the home-made machine. This allows to observe the *bulk* of the material during the traction experiment, and digital pictures (up to 1000 frames per second) may be recorded *via* a fast CCD camera (MotionScope 1000S, Redlake, USA) with an optical field and a pixel resolution (up to  $480 \times 420$ , 1-byte) depending on the chosen acquisition rate.

The fixed plate in the commercial machine is a square piece of anodized aluminum alloy. The probe is either microscope slide glass or stainless steel (machine tool adjusted).

### 3.2 Materials

In this study, we have used a non-volatile silicon oil provided by Rhodia Silicones (France): Rhodorsil gomme AS 522 (in short G20M), with a nominal viscosity of  $20 \cdot 10^3 \text{ Pa s}$ .

Rheological curves have been determined at room temperature using a controlled-stress rheometer (AR2000, TA Instruments, USA), in a cone-plate geometry (diameter= 20mm and angle= 4degrees). Two types of experiments have been conducted: oscillatory experiments (in the linear regime) and steady state flow measurements. Results are presented on figures 6, 7 and 8.

Figure 6 shows the linear viscoelasticity experiment. The sample displays an elastic behaviour ( $G' > G''$ ) at short times and a viscous behaviour ( $G'' > G'$ ) at long times. The corresponding characteristic time can be defined, for instance, by the value  $2\pi/\tau_{\text{crossing}}$  of  $\omega$  for which  $G'$  and  $G''$  have equal values.

The Cole-Cole diagramme presented on figure 7 shows that the rheology of the sample displays a Maxwell behaviour up to  $\omega \simeq 0.032 \text{ Hz}$ . We have extrapolated the Maxwell behaviour and determined a characteristic time  $\tau_{\text{Maxwell}}$ , a plateau modulus  $G_0$  and a viscosity ( $\eta = G''/\omega$ ) (see lines on figure 6 and on table 1).

Figure 8 displays the viscosity during steady state flow. The low-shear viscosity is  $\eta_{\text{stat.}} \simeq 20100 \text{ Pa.s}$ . This viscosity is similar to the viscosity measured by viscoelastic experiment ( $\eta_{\text{Maxwell}} \simeq 20770 \text{ Pa.s}$ ) and is consistent with nominal viscosity  $\eta_{\text{nominal}} = 20000 \text{ Pa.s}$ .

We have also tested some non-linear aspect of the G20M rheology. At high shear rate, the sample undergoes bulk cracks and it becomes impossible to measure the viscosity in the steady state flow experiment. However, assuming that the steady-shear viscosity can be deduced from the oscillatory viscosity ("Cox-Merz's" rule [18]), we can infer strong shear-thinning, see figure 8 (we could measure only about 10% shear-thinning directly in steady-shear). Such behaviour had been encountered with lower molecular weight silicon oils [9]. For oil G20M, the critical shear rate for the onset of shear-thinning, determined as the crossover between the asymptotic scaling laws for  $\eta(\dot{\gamma})$ , is  $\dot{\gamma}_c \simeq 1.55 \text{ Hz}$ .

Table 1 summarizes all above results. Silicone oil G20M obviously does not have one single relaxation time. In section 5, we shall nevertheless model it as a Maxwell fluid to account for the presence of both elastic (at high frequencies) and viscous (at low frequencies) behaviours.

|      | $\eta_{Mw} \text{ (Pa s)}$ | $\tau_{Mw} \text{ (s)}$ | $G_0 \text{ (Pa)}$ | $\tau_{\text{crois}} \text{ (s)}$ | $\dot{\gamma}_c \text{ (s}^{-1}\text{)}$ |
|------|----------------------------|-------------------------|--------------------|-----------------------------------|--|
| G20M | 20770                      | 6.7                     | 3100               | 0.94                              | 1.55                                     |

Table 1: Rheological properties of silicone oil G20M.

### 3.3 Data processing

A traction apparatus is not infinitely rigid. In particular, the force transducer has a finite compliance. The carriage location  $\ell$  and sample thickness  $h$  do not differ by just a constant: the difference between them depends on force,  $F$ . Similarly, the sample thickening rate  $\dot{h}$  differs from the nominal traction velocity  $V = \dot{\ell}$  (this was first pointed out with a system in JKR geometry [19], then observed also in a flat geometry [10, 20]).

We assume a linear machine compliance,  $1/K$ :

$$h(t) = h_0 + V t - \frac{F(t)}{K} \quad (13)$$

where the carriage location during the traction on a sample of initial thickness  $h_0$  is written as  $\ell(t) = h_0 + V t$ . For this expression to be valid, the force experienced by the material must be

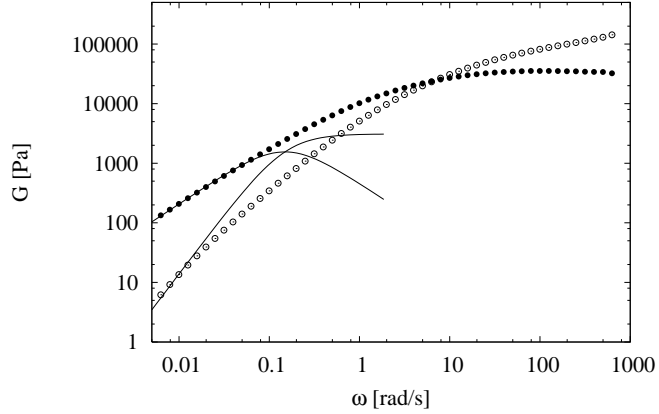


Figure 6: Linear, dynamic viscoelastic moduli  $G'(\omega)$  and  $G''(\omega)$  of G20M silicone oil. Open circles ( $\circ$ ) represent the elastic modulus  $G'$ , and close circles ( $\bullet$ ) the loss modulus  $G''$ . Both curves cross at  $\omega = \omega_{\text{crossing}} = 6.68 \text{ rad/s}$ . The full lines correspond to the moduli of a Maxwell fluid with a viscosity of  $\eta_{Mw} = 20770 \text{ Pa.s}$  and an elastic modulus  $G_0 = 3100 \text{ Pa}$ .

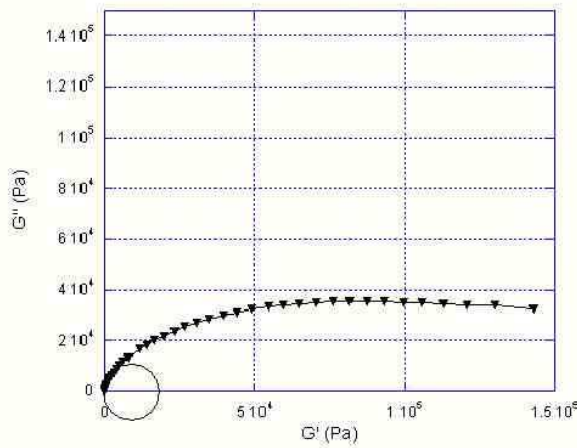


Figure 7: Cole-Cole diagramme for silicone oil G20M. The sample behaves like a Maxwell fluid up to  $\omega \simeq 0.032 \text{ rad/s}$ .

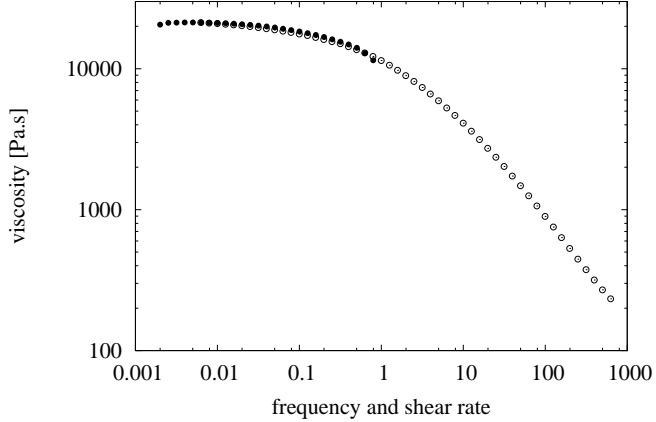


Figure 8: Viscosity of silicone oil G20M. Closed circles (●) represent the steady shear viscosity. Open circles (○) show the complex dynamic viscosity obtained from oscillatory experiments. They obey Cox-Merz's rule over the entire range of accessible steady shear (frequencies up to 0.9Hz).

fully relaxed to zero before traction starts: we systematically choose a long contact time  $t_c$ . There only remains a small, static capillary contribution to the force.

The compliance of each machine has been determined previously [9]:  $K = 4.5 \cdot 10^5$  N/m for the commercial machine and  $K = 2.5 \cdot 10^5$  N/m for the home-made prototype.

## 4 Results and interpretations

### 4.1 Results

In this study, the traction velocity is varied in the whole available range, from a few  $\mu\text{m/s}$  to a few  $\text{mm/s}$  and the thicknesses range from  $100\mu\text{m}$  to  $400\mu\text{m}$ . We have observed two types of curves:

- for low velocities or large thicknesses, the force decreases regularly after the initial force peak;
- for large velocities or small thicknesses, the force presents a peak, a plateau and a subsequent force drop.

Figure 9 displays some curves with a regular decrease and some curves with a plateau. Besides, we can observe that the plateau value increases with velocity.

Visual observation (see figure 11) shows that the transition between both types of force curves corresponds to the transition observed recently between fingering and cavitation mechanisms using less viscous silicone oils [9]. We won't discuss this effect in the present article.

At even higher traction velocities, (see figure 10), we observe that the plateau length decreases with increasing velocity, until it disappears at very high velocities. Besides, as will be described in more detail below, there is a transition in the amount of material that remains attached to the indenter when separation is complete (em cohesive versus adhesive failure).

This behaviour, which differs from the previous ones, may indicate the existence of yet another failure mechanism. We will now discuss these observations in greater detail.

### 4.2 Mechanism identification

Figure 12 shows three pictures taken successively during the traction of a silicone oil G20M sample with initial thickness  $200\mu\text{m}$  on the home-made prototype machine. It also schematically presents

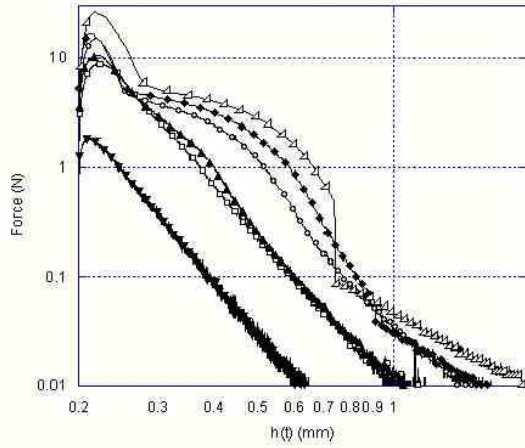


Figure 9: Traction curves for silicone oil G20M at low velocities:  $V = 0.001mm.s^{-1}$  ( $\blacktriangledown$ ),  $V = 0.008mm.s^{-1}$  ( $\square$ ),  $V = 0.01mm.s^{-1}$  ( $\blacktriangle$ ),  $V = 0.03mm.s^{-1}$  ( $\circ$ ),  $V = 0.05mm.s^{-1}$  ( $\blacklozenge$ ),  $V = 0.07mm.s^{-1}$  ( $\triangleright$ ).

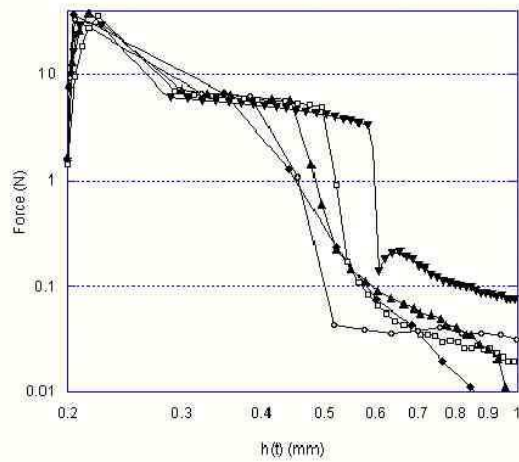


Figure 10: Traction curves for silicone oil G20M at high velocities:  $V = 0.2mm.s^{-1}$  ( $\blacktriangledown$ ),  $V = 0.5mm.s^{-1}$  ( $\square$ ),  $V = 0.7mm.s^{-1}$  ( $\blacktriangle$ ),  $V = 1.5mm.s^{-1}$  ( $\circ$ ),  $V = 2mm.s^{-1}$  ( $\blacklozenge$ ).

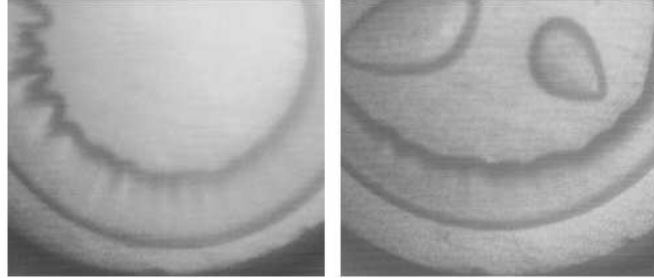


Figure 11: Photographs of silicone oil G20M taken with the home-made prototype in the course of traction. With traction velocity  $V = 0.02\text{mm/s}$  (left), viscous fingering is observed and the force curve decreases smoothly after the peak (not shown). At  $V = 0.05\text{mm/s}$  (right), cavitation is observed, as well as weakly developed viscous fingering. The force curve displays a plateau (full diamond data points (◆) on Figure 9).

our interpretation of the mechanisms observed. On the first picture, the sample appears as the medium grey disk. Traction causes the sample to retract (second and third photographs). As it retracts, it leaves a thin film of silicone oil on the plate. This appears as the dark annular region with constant outer radius. A bulk cavity is visible on the second picture (a white circle has been drawn around it for clarity). This cavity is expanding (see third picture). This is the cavitation mechanism observed previously [9].

Finally, yet another region can be seen on the third picture. It appears much brighter than the cavity. Besides, although its appearance and growth corresponds to a small increase in sample thickness, it has a large surface area. This suggests that it is thin. Moreover, we have noticed that after the experiment is complete, it corresponds to a place where the probe is free from any silicon oil. These observations lead us to believe that this region corresponds to an interfacial crack between the probe and the sample.

In summary, this example shows two different types of cavities. The first one develops in the bulk: this is genuine cavitation. The second one grows at the interface and remains flat: this is a crack.

### 4.3 Force curve interpretation: from cohesive failure to adhesive failure

#### 4.3.1 Origin of the plateau

Let us explain why the force curve displays a plateau, whether cavitation or cracks appear.

In a previous study [9], we have demonstrated that the existence of plateau in the case of bulk cavities is due to the difference between the very low pressure inside the bubbles and the atmospheric pressure outside the sample. The force drop after the plateau was interpreted as the penetration of air into the cavities.

The explanation is similar in the case of cracks: cracks do not contain any significant amount of gas, and they are isolated from the outside air by the presence of a silicone oil seal.

Let us now describe how the seal forms in practice. Figure 13 shows a force curve with a few photos taken at a high traction velocity, and the main stages of the unsticking process are schematically shown on figure 14.

A few small bubbles appear first (figure 14a and picture 1 on figure 13). Small cracks appear next (figure 14b and picture 2 on figure 13). Almost instantly, cracks then grow and merge into a unique crack (figure 14 and picture 3 on figure 13). The crack stops before it has reached the sample edge, thus leaving an annular region free of any bubbles or cracks near the edge. This is the *airtight seal*. Since the stress is now relieved, the bubbles shrink back and no further cavitation can be triggered. The plateau is free from any further events (see pictures 4 and 5 on figure 13).

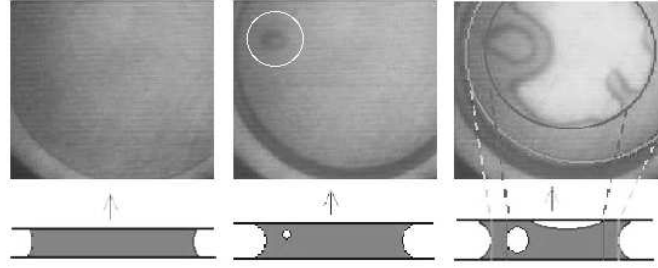


Figure 12: Cavitation, crack and airtight seal. These three pictures have been taken successively with the home-made prototype during traction (silicone oil G20M sample with thickness=200 $\mu$ m). The corresponding drawings expound our understanding of the mechanisms that take place in the sample. A bulk cavity is visible on the second picture (a white circle has been drawn around it for clarity). This cavity is expanding (see third picture). A whiter region can be seen on the third picture. It corresponds to a place where the probe is free from any silicon oil after the experiment is complete. These observations lead us to believe that this region corresponds to an interfacial crack between the probe and the sample. Two circles have been drawn on the third picture. The annular region between them is a free from any bubble or crack. It therefore isolates the inner region from the outside air and plays the role of an air-tight seal.

Hence, the seal (see figure 12) isolates the cavities and cracks (at quasi nil pressure) from the outside air (at atmospheric pressure). The airtight seal is thus essential for the existence of the force plateau.

The force remains important (plateau) as long as the seal resists the pressure difference. When the seal eventually breaks, air comes into the cavity formed by the crack, and the force decreases abruptly (time (6) on figure 13). The force drop corresponds to a pressure drop of roughly one atmosphere, as observed previously with cavitation [9].

#### 4.3.2 Plateau length

Figure 10 shows that the force plateau is shortened as the traction velocity is increased. This can be understood qualitatively as follows.

As the force drop is caused by air penetration [10, 9], we expect the duration of the plateau to depend on the resistance of the airtight seal. Now, figure 15 shows that the width of the airtight seal is reduced as the traction velocity is increased, which explains that the airtight seal then has a lower resistance. This reason for the decreased width of the airtight seal could probably be explained by a detailed theoretical analysis of the crack propagation in the present experimental conditions.

#### 4.3.3 Adhesive *versus* cohesive failure

The traction velocity not only affects the plateau length but also the nature of the failure between the adhesive and the indenter. Indeed, failure is observed to be adhesive in the region where the interfacial cracks have propagated, while it is observed to be cohesive in the airtight seal region. Hence, when traction velocity is increased, the annular region with cohesive failure becomes thinner. At very high velocities, interfacial cracks propagate right to the sample edge and no seal forms. Correspondingly, there is no plateau and the failure is purely adhesive (see figure 16).

The type of failure thus evolves from cohesive to partly adhesive and finally purely adhesive as the traction velocity is increased.

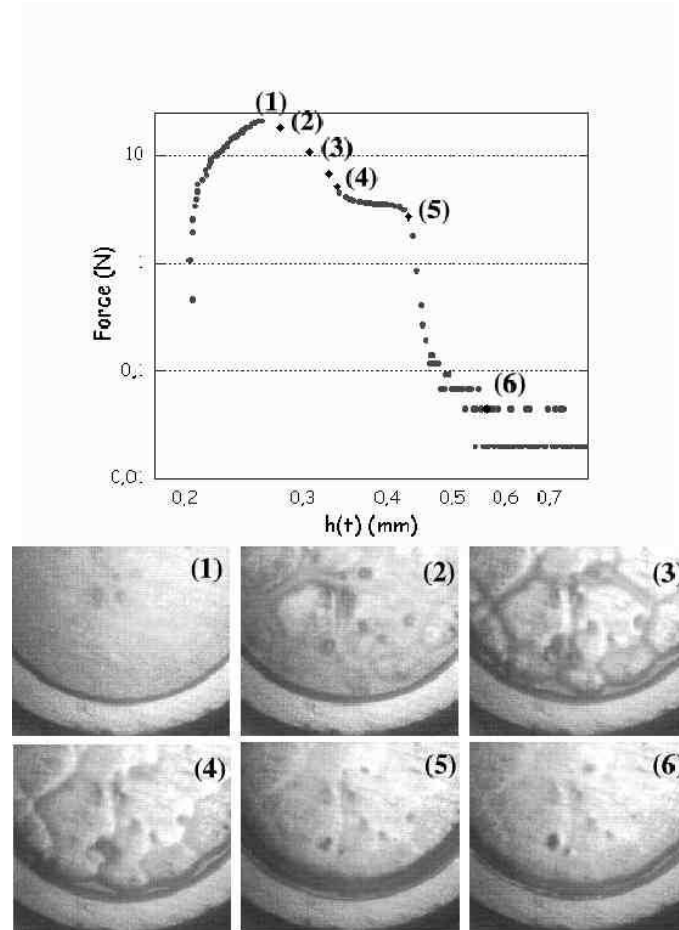


Figure 13: Traction curve for silicone oil G20M at a velocity of traction  $V = 1\text{mm/s}$  with the home-made prototype. The photos were taken at six times indicated on the curve. Cavities first appear (photos 1 and 2). Interfacial cracks then appear and propagate (from photo 2 onwards).

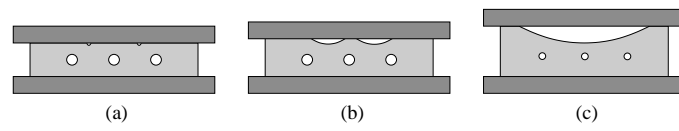


Figure 14: Major stages during separation. Some small cavities grow (a). Small interfacial cracks develop (b). The cracks quickly propagate further and merge, thus relaxing the tensile stress around the cavities, which therefore shrink back (c).

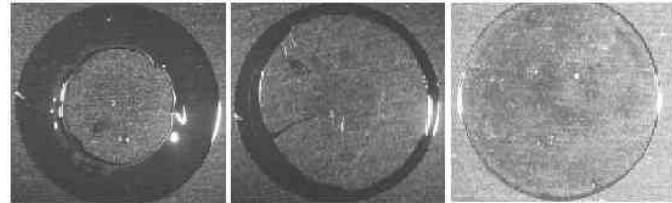


Figure 15: Sample aspect after complete separation for three different traction velocities (from left to right:  $V = 0.13\text{mm/s}$ ,  $V = 0.4\text{mm/s}$  and  $V = 0.7\text{mm/s}$ ). The width of the airtight seal area (dark gray), which isolates the interfacial crack region from the outside air, can be seen to decrease with increasing traction velocity.

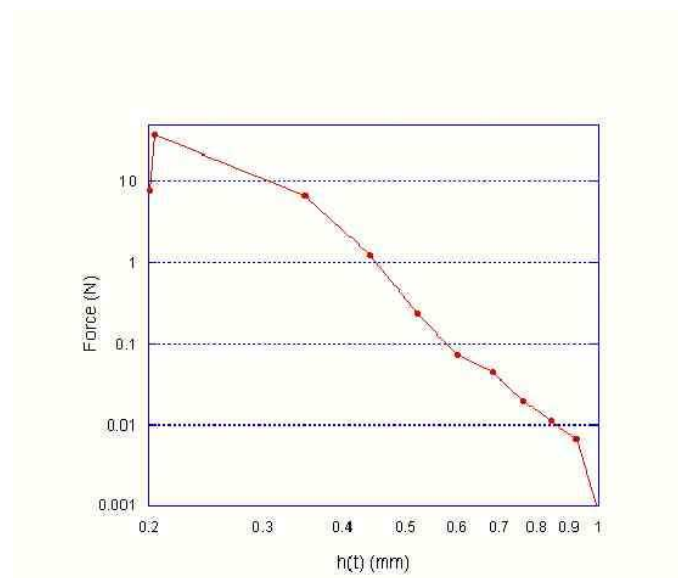


Figure 16: Force curve for a high traction velocity ( $V = 2\text{mm/s}$ ). No force plateau is to be seen.

#### 4.3.4 Conclusion of observations

Upon increasing the traction velocity with such highly viscous G20M silicone oil, crack was observed beyond fingering and cavitation. We described the crack appearance, growth and merging. At the sample edge, we observed the presence of an airtight seal after cracks have merged. The airtight seal isolates the crack region from the outside air. It is thus responsible for the observed force plateau. The width of the seal is observed to decrease as the traction velocity is increased, until it does not even form at very high velocities. One can infer that its resistance to the pressure difference between the crack and the outside air is weakened when its width is decreased. This is then consistent with the shorter force plateau. Only the crack region undergoes adhesive failure. Hence, the sample failure type evolves from cohesive to purely adhesive as the traction velocity is increased.

## 5 Model and discussion

As announced at the end of section 3.2, we model the sample behaviour as that of a Maxwell fluid with characteristic time  $\tau$ . In the present section, we derive the expected behaviour for such a fluid in the context of our experiment.

We first establish the evolution equation of the sample under traction (section 5.1). Therefrom, we then determine the main possible types of evolutions, independently of the failure mechanisms (section 5.2). We then introduce these failure mechanisms and discuss qualitatively how they may be triggered and how they orient the evolution of the system (section 5.3). It appears that in order to account for all observed phenomena, one must include the kinetics of cavitation (section 5.4). We then briefly discuss the triggering and propagation of interfacial cracks (section 5.5). Knowing the influence of cavitation and crack, we then establish the phase diagramme of the system in terms of the experimental parameters (section 5.6). We finally compare and discuss the theoretical predictions and the experimental measurements (section 5.7).

The experimental variables are listed in table 2 below, including in their adimensional version which we use in the remaining of this article.

|                         |   |   |
|-------------------------|---|---|
| $h$                     | $H = h/h_0$   | sample thickness  |
| $t$                     | $T = tV/h_0$  | time  |
| $F$                     | $\mathcal{F} = \frac{F}{Kh_0}$  | force   |
| $\frac{dh}{dt}$         | $\dot{H} = \frac{dH}{dT} = \frac{1}{V} \frac{dh}{dt}$                     | top plate velocity                                      |
| $\tau$                  | $T = \frac{V\tau}{h_0}$   | Maxwell fluid relaxation time                           |
| $\sigma$                | $\mathcal{F}H = \frac{Fh}{Kh_0^2}$  | average tensile stress                                  |
| $2\sigma$               | $2\mathcal{F}H = \frac{Fh}{Kh_0^2}$                                       | maximum tensile stress<br>(at the center of the sample) |
| $\sigma_{\text{seuil}}$ | $\Sigma^* = \sigma_{\text{seuil}} \frac{\pi a_0^2}{Kh_0^2}$               | failure threshold                                       |
| $t_{\text{cav}}$        | $T_{\text{cav}} = \frac{\pi p_{\text{atm}} a_0^2}{Kh_0}$                  | cavitation time   |
| $t_{\text{growth}}$     | $T_{\text{growth}} = \sqrt{\frac{8\pi\eta V a_0^2}{Kh_0^2}}$              | bubble growth time                                      |
| $t_{\text{crack}}$      | $T_{\text{crack}} = \frac{\pi a_0^2}{Kh_0} \sqrt{\frac{G\mathcal{W}}{b}}$ | crack time  |

Table 2: Adimensional variables

### 5.1 Evolution equation

We here present the essential ingredients that determine the sample evolution. A complete calculation is to be found in Appendix A.

If the material was purely elastic and homogeneous, with shear modulus  $G$ , the force would read:

$$F = \frac{3\pi}{2} a_0^4 h_0^2 G \frac{h - h_0}{h^5} \quad (14)$$

with non-dimensional version:

$$\mathcal{F} = C_{\text{el}} \frac{H - 1}{H^5} \quad (15)$$

where

$$C_{\text{el}} = \frac{3\pi}{2} \frac{G}{K} \frac{a_0^4}{h_0^3} \quad (16)$$

Parameter  $C_{\text{el}}$  is the ratio between the machine stiffness and the material elasticity (in our case,  $C_{\text{el}} \simeq 74$  for the commercial traction apparatus, with sample diameter  $2a_0 = 9.5\text{mm}$  and sample thickness  $h_0 = 200\mu\text{m}$ ).

Equation 15 describes a disk of elastic material under traction. Derivating it with respect to time  $T$  yields, when  $H - 1 \ll 1$ :

$$\dot{\mathcal{F}} = C_{\text{el}} \frac{\dot{H}}{H^5} \quad (17)$$

If the purely elastic material is replaced with a Maxwell fluid ( $G\tau = \eta$ ), it is shown in Appendix A that  $\dot{\mathcal{F}}$  is simply replaced with  $\dot{\mathcal{F}} + \mathcal{F}/\mathcal{T}$ :

$$\dot{\mathcal{F}} + \frac{\mathcal{F}}{\mathcal{T}} = C_{\text{el}} \frac{\dot{H}}{H^5} \quad (18)$$

where  $\mathcal{T}$  is the non-dimensional Maxwell time (see Table 2).

Note that neglecting the elastic term  $\dot{\mathcal{F}}$  and keeping only the viscous term  $\mathcal{F}/\mathcal{T}$  in Equation (18) yields the Stefan equation [21] used in our previous model [9]:

$$\mathcal{F} = C \frac{\dot{H}}{H^5} \quad (19)$$

where

$$C \equiv C_{\text{el}} \mathcal{T} = \frac{3\pi}{2} \frac{\eta V}{K} \frac{a_0^4}{h_0^4} \quad (20)$$

is the ratio between the machine stiffness and the resistance of the sample once it has turned liquid.

The force expressed by Equation (18) is transmitted by the machine, which behaves like a spring:

$$\mathcal{F} = 1 + T - H \quad (21)$$

where  $1 + T$  is the motor position, and  $H$  that of the upper plate. By combining equation 21, as well as its time derivative, with equation 18, one obtains the evolution equation for a disk of a Maxwell fluid under traction:

$$T \left( C_{\text{el}} \frac{\dot{H}}{H^5} + \dot{H} - 1 \right) = \mathcal{F} = 1 + T - H \quad (22)$$

This is the central equation in our model. In the absence of any cavitation or crack, it yields the evolution of the sample thickness,  $H(T)$ , and that of the force,  $\mathcal{F}(T)$ , starting with initial condition  $H = 1$  at  $T = 0$ . Graphically, both quantities can be visualized very simply, as their sum is the uniformly varying motor position (see Figure 17).

## 5.2 Main types of evolution

Starting with initial condition  $H = 1$  at  $T = 0$ , we now study the various types of system behaviours, in the absence of cavitation or crack. Only in section 5.3 will we study crack and cavitation.

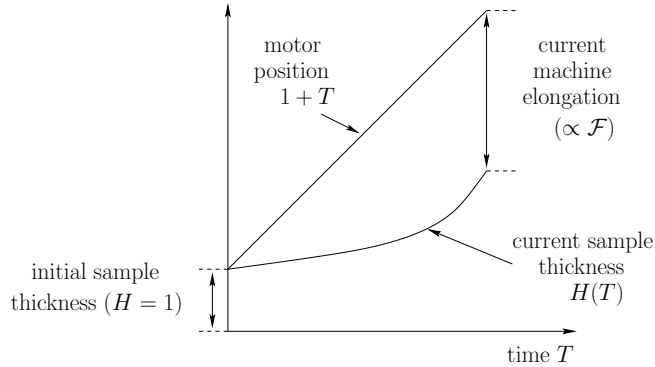


Figure 17: Schematic representation of the system behaviour. The motor position  $1 + T$  and the sample thickness  $H(T)$  are plotted as a function of time. The difference between the motor position and sample thickness values is the machine elongation; it is proportional to the force  $\mathcal{F}$  that is transmitted through the sample, as expressed by Equation (21).

### 5.2.1 Viscous regimes

Two types of behaviours have already been described in our previous work, dealing with purely viscous liquids [9]. Example solutions are depicted on Figure 18. Beside numerical solutions to Equation (22), analytical approximate solutions can be obtained for various stages of the system's evolution in order to provide insight into the system's behaviour. The corresponding analytical expressions for the main variables are provided in Table 4.

For low values of  $C = C_{\text{el}}\mathcal{T}$  (dotted curve on Figure 18), the sample remains still for a short period of time (stage  $V3$ ); it then follows the motion of the motor very closely (stages  $V4$  and  $V6$ ).

By contrast, for large values of  $C$  (full curve on Figure 18), the sample remains still for a longer period of time while the machine elongates and the force rises (stage  $V3$ ); only later does it suddenly flow and relieve the force (stage  $V5$ ) while the upper plate catches up with the current motor position; it eventually follows the motion of the motor closely (stage  $V6$ ).

Beside these viscous regimes, the elastic components of equation (22) have several consequences, which we now discuss.

### 5.2.2 Elastic behaviour at short times

When  $\dot{\mathcal{F}} = 1 - \dot{H}$  is much larger than  $\mathcal{F}/\mathcal{T}$ , the evolution equation (22) reduces to its elastic version (equation 15). As shown in Appendix A, this occurs — unsurprisingly — at rather short times ( $T \ll \mathcal{T}$ ).

When this elastic behaviour at short times is taken into account, the succession of stages depicted on Figure 18 becomes richer, see Figure 19.

The viscous stages, labeled  $V3$  to  $V6$ , now follow elastic stage  $E1$ ; correspondingly, the regimes discussed above are labeled  $R1346$  (for  $C \ll 1$ ) and  $R1356$  (for  $C \gg 1$ ).

Also, a third route has appeared, labeled  $R246$ , which consists in elastic stage  $E2$  followed by viscous stages  $V4$  and  $V6$ . Furthermore, equation (22) can become invalid if large deformations are reached while the sample still behaves elastically, (*i.e.*, prior to time  $T \simeq \mathcal{T}$ ). Let us now consider both issues: the existence of two distinct elastic stages at short times, and the possible onset of large elastic deformations.

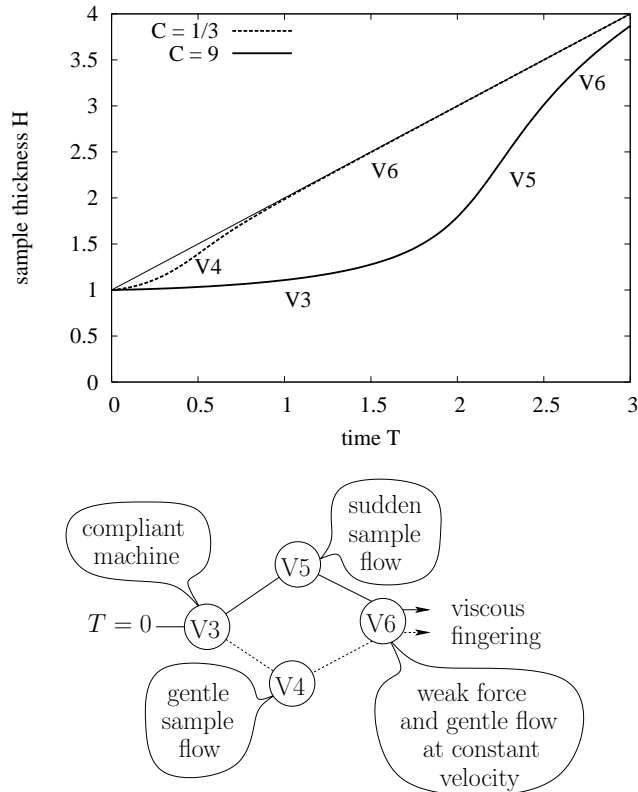


Figure 18: System evolution when the sample is essentially viscous. Top: sample thickness as a function of time. Bottom: schematic succession of stages. When  $C \ll 1$ , the machine elongation  $1 + T - H$  remains much smaller than the sample thickness  $H$  at all times: stage  $V3$  (at short times) is soon followed by stages  $V4$  and  $V6$ , as illustrated by the dotted curve, obtained from equation (22) with  $C = 1/3$  and  $C_{\text{el}} = 5.2$ . By contrast, when  $C \gg 1$ , stage  $V3$  extends over a longer period of time and the machine elongates much further; stages  $V5$  and  $V6$  then relieve the traction force, as illustrated by the full curve, obtained with  $C = 9$  and  $C_{\text{el}} = 27$ . These two regimes, studied in our previous work [9] devoted to Newtonian fluids, correspond to the limit  $C_{\text{el}}^2/C \rightarrow \infty$  in the present context of a Maxwell fluid. See Table 4 for approximate analytical expressions for the main variables during stages  $V3$  to  $V6$ .

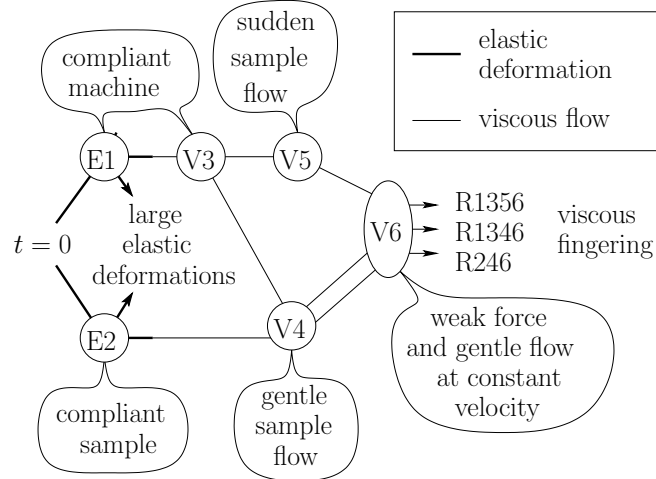


Figure 19: Various possible sequences of stages (from  $E1$  or  $E2$  to  $V6$ ). Regimes  $R1356$ ,  $R1346$  and  $R246$  are the three evolution *scenarii* for the Maxwellian system in the absence of any cavitation or crack. The case where large deformations are reached while the sample behaves elastically would require further assumptions and is not addressed in the present work.

### 5.2.3 Compared machine and sample compliance

At very short times, when the sample thickness is still close to its initial value ( $H \simeq 1$ ), one can combine equations (15) and (21) and show that the evolution of the thickness and force is linear:

$$H - 1 \simeq T \frac{1}{1 + C_{el}} \quad (23)$$

$$\mathcal{F} \simeq T \frac{C_{el}}{1 + C_{el}} \quad (24)$$

These equations reflect the fact that the deformation induced by the uniform motor motion (displacement  $T$ ) is shared between the sample ( $H - 1$ ) and the machine ( $\mathcal{F}$ ), according to the ratio  $C_{el}$  of their respective elastic compliances. As a result, elastic stage  $E1$  or  $E2$  arises at short times, depending on the value of  $C_{el}$ .

In stage  $E1$  (with  $C_{el} \gg 1$ ), the machine is more compliant than the sample: the sample deforms at a much lower velocity than the motor velocity ( $\dot{H} \ll 1$ , see Table 4 in Appendix B). Correspondingly, in regime  $R1346$  of Figure 20, the curve  $H(T)$  starts with a horizontal tangent.

By contrast, in stage  $E2$  (with  $C_{el} \ll 1$ ), the sample is more compliant than the machine and deforms almost at the motor velocity ( $\dot{H} \simeq 1$ ), and the curve  $H(T)$  in regime  $R246$  of Figure 20 starts with a slope almost equal to one.

### 5.2.4 Large elastic deformations

The elastic behaviour is well described by equations (23) and (24), which are linear, when the shear deformation of the material in the gap is small. The shear deformation in the material is maximal at the edge and near the plates. It is equal to the product of the relative thickening ( $h - h_0$ )/ $h_0$  and of the aspect ratio  $a/h$ :

$$\gamma = (H - 1) \frac{a}{h} \quad (25)$$

Large deformations are reached when  $\gamma$  becomes of order unity. Since  $a/h$  is much larger than unity, this occurs when  $H - 1$  is still small. Hence, we can use the initial aspect ratio,  $a_0/h_0$  in equation (25).

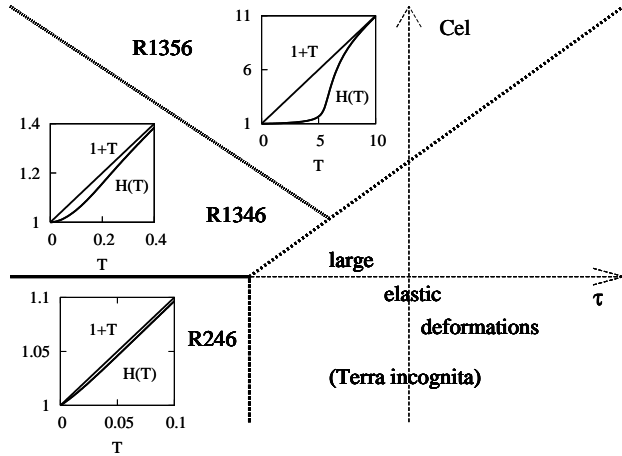


Figure 20: System behaviour depending on experimental parameters  $T$  and  $C_{\text{el}}$  (see equations 16 and 18). Regimes  $R1346$  and  $R1356$ , obtained when  $C_{\text{el}}/T \gg a_0/h_0$  and  $C_{\text{el}} \gg 1$ , result from the viscous behaviour of the sample coupled to the machine compliance, as described for a Newtonian fluid [9]. In the present situation of a Maxwell fluid, the succession of stages in the system behaviour is richer (see Figure 19). In regime  $R246$ , obtained when the machine is very rigid, the sample thickness follows the motor motion almost exactly. Finally, for large  $T$  (see equation 26), the sample reaches large deformations while still elastic. This regime is beyond the scope of the present work, as it would require additional assumptions concerning the mechanical properties of the material.

Equation 23 indicates that whenever

$$T > \frac{h_0}{a_0}(1 + C_{\text{el}}), \quad (26)$$

large deformations are reached before the material flows (*i.e.*, while  $T < T$ ).

Large elastic deformations cannot be addressed in the framework of linear elasticity. Treating them would require additional hypotheses on the material behaviour, which goes beyond the scope of the present article. The regime where such large elastic deformations occur is indicated on figure 20.

### 5.3 Triggering the failure mechanisms

We have now determined the evolution of the system from equation (22), *i.e.*, in the absence of cavitation or crack. The results are summarized in Figures 19 and 20 and in Table 4.

Let us now use the results of Section 2 to determine which regions of Figure 20 correspond to cavitation or crack.

#### 5.3.1 Pressure as the triggering variable

As discussed in Section 2, the relevant variable to determine when cavitation or crack should develop is the (tensile) pressure contribution due to traction. Since it is non-homogeneous in the sample, we take the highest value in the sample, which is in the center of the sample and equal to twice its average value. It is therefore equal to  $2F/(\Omega/h)$ . In non-dimensional form, as indicated in Table 2, it is given by the product  $2\mathcal{F}H$ . Cavitation or crack is expected to develop when the value of this product exceeds the corresponding threshold determined in Section 2.

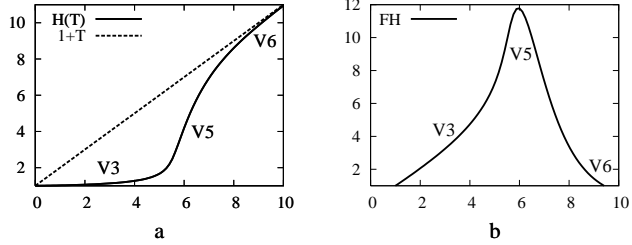


Figure 21: Sample thickness  $H(T)$  (left-hand side) and tensile stress  $FH(T)$  (right-hand side) in regime R1356 (see Figure 20), with stages  $E1$  (elastic),  $V3$  (viscous),  $V5$  (catching up) and  $V6$  (weak force and constant velocity flow).

The value of  $2FH(T)$  can be determined by solving differential equation (22) numerically. In order to determine the main regimes, however, it is sufficient to consider the expressions of  $FH(T)$  during the various stages, which are given in Table 4 of Appendix B).

### 5.3.2 Importance of the failure mechanism kinetics

As a first approach, one might assume that whenever cavitation or crack is triggered, due to sufficient tensile stress, it relaxes the stress instantaneously. The experimental results presented on figure 9, as well as our earlier study [9], would seem to justify this assumption.

However, our recent observations (see parts 4.2 and 4.3) show that above some traction velocity, cracks appear *after* cavitation has started. This observation has two implications:

- the cavitation threshold is lower than the crack threshold (indeed, cavitation appears first);
- the stress relaxation induced by the cavity growth is not instantaneous.

To understand these observations, we therefore need to take into account the kinetics of the cavity growth and determine its consequences on the stress evolution in the sample.

### 5.3.3 Decorative *versus* effective cavitation

Before we determine their growth rate, let us emphasize the fact that the cavity growth has two main consequences:

- the cavity soon becomes visible (once it is around one micron in size);
- the cavity later has a mechanical effect on the system (once its size has become comparable to the sample thickness, *i.e.* around one hundred microns).

Since the required sizes for visibility and for mechanical effectiveness are very different, it may happen to be relevant to consider the period of time when the cavity is visible though not mechanically active. This stage is then called “decorative cavitation”, as illustrated on figure 22.

### 5.3.4 Paths towards failure

Depending on the growth kinetics, “decorative” cavitation may or may not play a significant role in the development of failure mechanisms. As a result, if we consider for instance viscous regime V3 as a starting point, various failure regimes can be expected, as described on Figure 23.

If the crack threshold is lower than the cavitation threshold, only cracks are observed (regime R139).

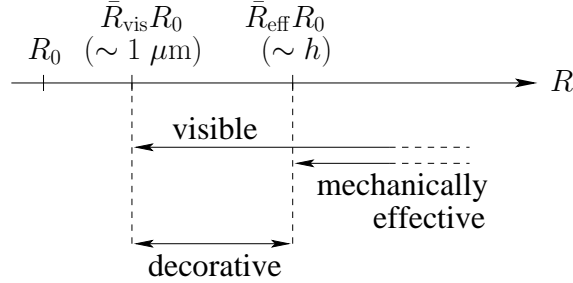


Figure 22: Visibility and mechanical role of bulk cavities as they grow from their initial size  $R_0$  to their final, macroscopic size. As soon as their size exceeds about one micron, they become visible. They are not mechanically effective in relieving the tensile stress, however, until their size becomes comparable to the sample thickness. In the mean time, they can be adequately described as purely “decorative”.

Otherwise, cavities appear and reach a visible dimension (decorative stage  $V7$ ). The fate of the system then depends on the cavity growth rate:

- If viscosity is low, cavities grow very quickly and cavitation can be considered instantaneous (regime  $R138$ ).
- If viscosity is high, cavities remain decorative for a long time and effective cavitation is delayed (regime  $R1378$ ).
- If viscosity is even higher, cracks may be triggered (stage  $C9$ ) while cavities are already visible (regime  $R1379$ ).

Let us now study in detail the kinetics of the cavity growth.

## 5.4 Kinetics of cavitation

Cavitation in an infinite and purely elastic medium was described by Gent and collaborators [12, 13]. Recently, this approach was extended to the case of a finite sample [22, 23] to determine the final cavity size.

In the present article, we essentially study cavities that appear in a viscous sample. Cavitation kinetics will thus be addressed only in the viscous stages described above:  $V3$ ,  $V4$ ,  $V5$  and  $V6$  (see paragraph 5.2.1). As mentioned elsewhere [9], the kinetics of the microbubble growth (initial radius  $R_0$ ) is governed by equation [24]:

$$\frac{\dot{R}}{R} = \frac{p_{\text{eq}}(R) - p(t)}{4\eta} \quad (27)$$

In this equation,  $p(t)$  is the pressure in the sample as determined in the absence of cavitation, and  $p_{\text{eq}}(R)$  is the pressure at which a bubble of radius  $R$  is in mechanical equilibrium with its surroundings:

$$p_{\text{eq}}(R) = \frac{R_0^3}{R^3} \left[ p_{\text{atm}} + \frac{2\gamma}{R_0} \right] - \frac{2\gamma}{R}, \quad (28)$$

The shape of function  $p_{\text{eq}}(R)$  yields a pressure threshold [9] (see figure 24 for an illustration) which corresponds to a tensile contribution slightly greater than  $p_{\text{atm}}$  in our case, as mentioned in paragraph 5.5.2.

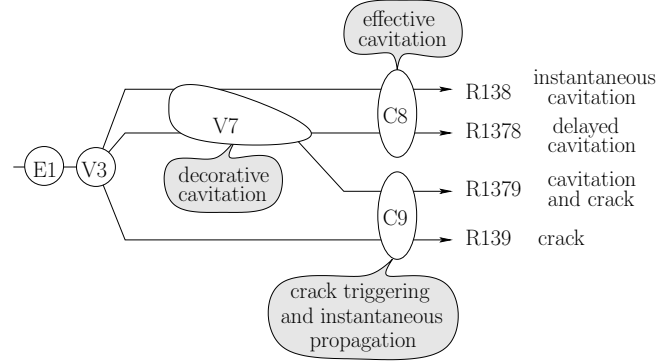


Figure 23: Various failure regimes expected to be triggered during viscous regime  $V3$ , taking into account the kinetics of cavity growth. If the cavitation threshold is lower than the crack threshold, cavities start to grow and soon become visible: they are decorative (stage  $V7$ ). If viscosity is low (uppermost path), the cavities grow very quickly and become mechanically effective (stage  $C8$ ); thus, the duration of the decorative stage is negligible and cavitation can be considered instantaneous (regime  $R138$ ). By contrast, if viscosity is high, cavities remain decorative for a long time and effective cavitation is delayed (regime  $R1378$ ). If viscosity is even higher, as the tensile stress continues to increase during the decorative stage  $V7$ , cracks may be triggered (stage  $C9$ ). If cracks develop fast, they relieve the stress and hinder any further cavity growth. Hence, cavitation is observed for some time, but eventually cracks take over (regime  $R1379$ ). Finally, if the crack threshold is lower than the cavitation threshold, then the system evolves directly from  $V3$  to  $C9$ . Only cracks are observed (regime  $R139$ ).

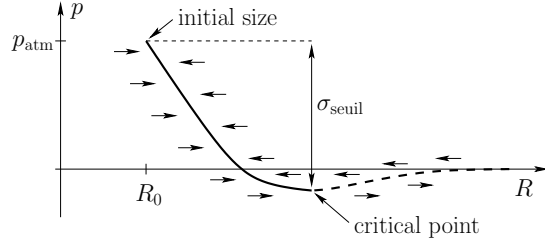


Figure 24: Conditions of stability and growth of a bulk cavity, depending on the external pressure. The curve is a schematic representation of function  $p_{\text{eq}}(R)$  given by equation (28). The evolution of the bubble size (illustrated by horizontal arrows) is determined by equation (27). It implies that the first part of the curve (solid line) is a stable branch, while the second part (dashed line) is unstable. The corresponding critical point determines the quasistatic pressure threshold.

#### 5.4.1 Non-dimensional cavity growth equations

In non-dimensional form, equations (27) and (28) read:

$$\frac{d\bar{R}}{dT} = A \bar{R} [2\mathcal{F}H(T) - \Sigma_{\text{eq}}(\bar{R})] \quad (29)$$

$$\begin{aligned} \Sigma_{\text{eq}}(\bar{R}) = & \frac{\pi a_0^2 p_{\text{atm}}}{K h_0} \left[ \left(1 - \frac{1}{\bar{R}^3}\right) \right. \\ & \left. + \frac{2\gamma}{R_0 p_{\text{atm}}} \left(\frac{1}{\bar{R}} - \frac{1}{\bar{R}^3}\right) \right] \end{aligned} \quad (30)$$

where  $\bar{R} = R/R_0$  and:

$$A = \frac{K h_0^2}{4\pi a_0^2 \eta V} = \frac{3}{8} \frac{1}{C} \frac{a_0^2}{h_0^2} \quad (31)$$

(32)

Here,  $\Sigma_{\text{eq}}$  is the non-dimensional form of  $p_{\text{atm}} - p_{\text{eq}}$ , and  $C$  is the constant defined by equation (20) [9]. Note the factor 2 in term  $2\mathcal{F}H(T)$  in equation (29). It reflects the fact that the pressure (tensile) component due to the fluid flow is non-homogeneous in the sample and that in the center of the sample, it is equal to twice its average value.

#### 5.4.2 Cavity growth in the present experimental context

As indicated in Table 4,  $\mathcal{F}H(T)$  is of order  $T$  in regimes *E1* and *V3*.

The main trends of the cavity growth depend essentially on the initial slope  $B$  and on the maximum value  $\Sigma_c$  of function  $\Sigma_{\text{eq}}(\bar{R})$ :

$$B = \left. \frac{d\Sigma_{\text{eq}}(\bar{R})}{d\bar{R}} \right|_{\bar{R}=1} = \frac{3\pi a_0^2 p_{\text{atm}}}{K h_0} \left[ 1 + \frac{4\gamma}{3R_0 p_{\text{atm}}} \right] \quad (33)$$

$$\Sigma_c = \frac{\pi a_0^2 p_{\text{atm}}}{K h_0} \left[ 1 + \frac{2}{3\sqrt{3}} \frac{\left( \frac{2\gamma}{R_0 p_{\text{atm}}} \right)^{3/2}}{\sqrt{1 + \frac{2\gamma}{R_0 p_{\text{atm}}}}} \right] \quad (34)$$

Note that  $B$  and  $\Sigma_c$  differ by a numerical factor which evolves in a limited range of values:

$$3 < \frac{B}{\Sigma_c} < 3\sqrt{3} \quad (35)$$

where the lower value, 3 corresponds to the limit  $\gamma \ll R_0 p_{\text{atm}}$ , and the greater value,  $3\sqrt{3}$ , to the opposite limit,  $\gamma \gg R_0 p_{\text{atm}}$ .

#### 5.4.3 Cavity growth parameter

When solving Equation (29) for  $\bar{R}(T)$ , it appears that the dynamics of the cavity growth depends qualitatively on the value of parameter

$$\Sigma_c \sqrt{A} = \frac{\sqrt{\pi}}{2} \frac{a_0 p_{\text{atm}}}{\sqrt{K \eta V}} \left[ 1 + \frac{2}{3\sqrt{3}} \frac{\left( \frac{2\gamma}{R_0 p_{\text{atm}}} \right)^{3/2}}{\sqrt{1 + \frac{2\gamma}{R_0 p_{\text{atm}}}}} \right] \quad (36)$$

This parameter is indeed relevant in our set of experiments. For the  $\eta = 10^3$  Pa.s oil, with  $a_0 = 5$  mm,  $p_{\text{atm}} = 10^5$  Pa,  $K = 2 \cdot 10^5$  N/m, taking a large traction velocity  $V = 1$  mm/s and assuming  $\gamma/R_0 \ll p_{\text{atm}}$ , one gets  $\Sigma_c \sqrt{A} \simeq 1$ . Thus, as mentioned in our earlier work [9], the viscosity-delayed cavity growth appears even for an oil with viscosity  $\eta = 10^3$  Pa.s at large traction velocities. *A fortiori*, the cavity growth parameter  $\Sigma_c \sqrt{A}$  takes small values with our more viscous oil ( $\eta = 2 \cdot 10^4$  Pa.s).

#### 5.4.4 Instantaneous cavity growth

At low traction velocities ( $\Sigma_c \sqrt{A} \gg 1$ ), well before the cavitation threshold is reached ( $T = \Sigma_c/2$ ), Equation (29) can be approximated as  $d\bar{R}/dT = A\bar{R} [2TH - B\bar{R}]$  by using  $\mathcal{F} = T$  and  $\Sigma_{\text{eq}} = B\bar{R}$ . Hence, the cavity growth is mainly linear at short times, as illustrated on Figure 25:

$$\bar{R} \simeq 1 + \frac{2T}{B} - \frac{2}{AB^2} (1 - e^{-ABT}) \simeq 1 + \frac{2T}{B} \quad (37)$$

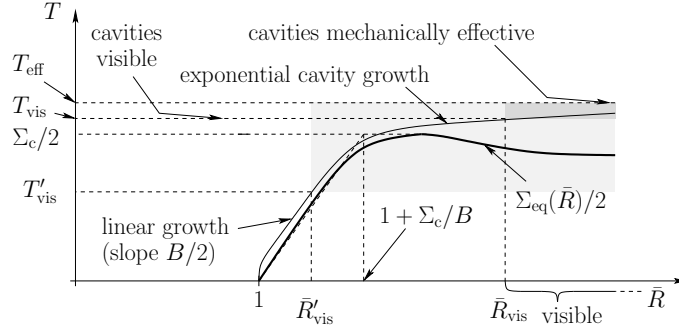


Figure 25: Cavity evolution (time  $T$ , radius  $\bar{R}$ ) under low traction velocity ( $\Sigma_c \sqrt{A} \gg 1$ ): instantaneous cavity growth. In this regime, the cavity grows at first linearly ( $T < \Sigma_c/2$ ), then much more rapidly (exponential growth). When the initial cavity is much too small to be visible ( $\bar{R}_{\text{vis}} \gg 1$ ), the observable growth (medium grey region) is thus very rapid ( $T_{\text{vis}} < T < T_{\text{eff}}$ ). By contrast, if the cavity is initially almost visible ( $\bar{R}_{\text{vis}} < 1 + \Sigma_c/B$ ), then the duration of the observable growth is longer (light grey), and a substantial part of the growth is essentially linear ( $T'_{\text{vis}} \leq T < \Sigma_c/2$ ).

At later times ( $T > \Sigma_c/2$ ), the cavity radius increases exponentially.

As a result, the time  $T_{\text{eff}}$  at which the cavities have a mechanical effect (see figure 22) is essentially equal to  $\Sigma_c/2$ :

$$T_{\text{eff}} \simeq \frac{\Sigma_c}{2} + \sqrt{\frac{1}{A} \log \left( \frac{\bar{R}_{\text{eff}}}{1 + \Sigma_c/B} \right)} \simeq \frac{\Sigma_c}{2} \quad (38)$$

As for the time  $T_{\text{vis}}$  at which cavities become visible (radius  $\bar{R}_{\text{vis}}$ ), it depends on how  $\bar{R}_{\text{vis}}$  compares with  $1 + \Sigma_c/B$ , as illustrated on Figure 25.

If the cavity is initially very small and thus needs to grow substantially before it becomes visible ( $\bar{R}_{\text{vis}} \gg 1 + \Sigma_c/B$ ), then  $T_{\text{vis}}$  is also on the order of  $\Sigma_c/2$ , and the cavity remains decorative (see figure 22) only very briefly:

$$T_{\text{eff}} - T_{\text{vis}} = \mathcal{O} \left( \frac{1}{\sqrt{A}} \right) \ll \frac{\Sigma_c}{2} \simeq T_{\text{vis}} \simeq T_{\text{eff}} \quad (39)$$

By contrast, if the initial cavity is almost visible, *i.e.*,  $1 < \bar{R}_{\text{vis}} < 1 + \Sigma_c/B$  (or already visible, with  $\bar{R}_{\text{vis}} < 1$ ), then it is possible to observe a slow, mainly linear cavity growth from  $T = T_{\text{vis}}$  to  $T \simeq \Sigma_c/2$ , with  $T_{\text{vis}} \simeq B(\bar{R}_{\text{vis}} - 1)/2$  (or  $T_{\text{vis}} = 0$ , respectively).

#### 5.4.5 Delayed cavity growth

At high traction velocities ( $\Sigma_c \sqrt{A} \ll 1$ ), the cavity growth is exponential<sup>5</sup> and becomes substantial only *well after* the cavitation threshold ( $T = \Sigma_c/2$ ) has been reached, as illustrated on Figure 26:

$$\bar{R} \simeq e^{+A T^2} \quad (40)$$

<sup>5</sup>This can be shown by considering inequality  $0 \leq \Sigma_{\text{eq}}(\bar{R}) \leq \Sigma_c$ . Combined with equation

$$\frac{dT}{d\bar{R}} = \frac{1}{A \bar{R} [2\mathcal{F}H(T) - \Sigma_{\text{eq}}(\bar{R})]},$$

it implies that  $\frac{1}{A\bar{R}^2 T} \leq \frac{dT}{d\bar{R}} \leq \frac{1}{A\bar{R}(2T - \Sigma_c)}$ , and hence that:

$$\sqrt{\frac{1}{A} \log \bar{R}} \leq T(\bar{R}) \leq \Sigma_c + \sqrt{\frac{1}{A} \log \bar{R}}$$

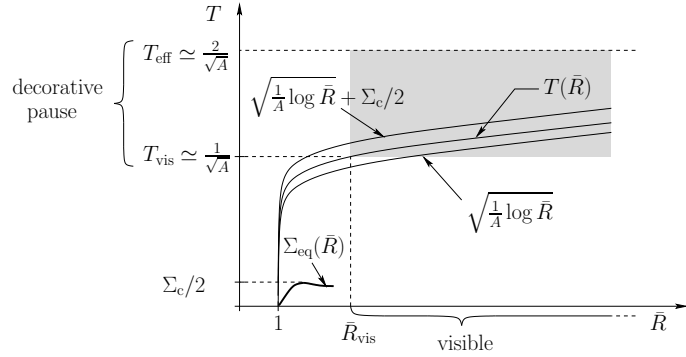


Figure 26: Cavity evolution (time  $T$ , radius  $\bar{R}$ ) under large traction velocity ( $\Sigma_c \sqrt{A} \ll 1$ ): delayed cavity growth. In this regime, the cavity growth is delayed by the fluid viscosity. The cavity radius increases essentially like  $e^{+A T^2}$ . As a result, there is a substantial time lag (“decorative pause”) between the time  $T_{\text{vis}}$  at which the cavity becomes visible and the time  $T_{\text{eff}}$  at which it becomes mechanically effective (see figure 22).

In other words, the cavity growth is substantially delayed by the fluid viscosity, hence the term *delayed cavitation*. The time for visible and effective cavitations are then given by:

$$T_{\text{vis}} \simeq \sqrt{\frac{\log \bar{R}_{\text{vis}}}{A}} \quad (41)$$

$$T_{\text{eff}} \simeq \sqrt{\frac{\log \bar{R}_{\text{eff}}}{A}} \quad (42)$$

i.e., typically:

$$T_{\text{vis}} \sim \frac{1}{\sqrt{A}} \quad (43)$$

$$T_{\text{eff}} \sim \frac{2}{\sqrt{A}} \quad (44)$$

In other words, in this regime of high traction velocity, the system marks a significant “decorative pause” and thus paves the way for a treacherous crack attack on cavity growth (see Figure 23).

#### 5.4.6 Cavity growth during stage V4

Among viscous stages  $V3$  to  $V6$ , only stages  $V3$  and  $V5$  correspond to increasing tensile pressure (see Table 4) and are thus suitable for triggering cavitation.

Yet, in the regime of delayed cavitation, once the threshold pressure has been reached ( $T > \Sigma_c/2$ ), the system may evolve from stage  $V3$  to stage  $V4$  (at time  $T \sim C$  during route R1346) and still drive cavity growth. As the tensile pressure is constant during stage  $V4$  (with  $2\mathcal{F}H \simeq 2C$ , see Table 4), the exponential cavity growth law is somewhat altered as compared to equation (40):

$$\bar{R}(T) \sim e^{+2A C T} = e^{\frac{3}{4} \frac{a_0^2}{h_0^2} T} \quad (45)$$

Hence, the times for cavities to become visible or mechanically effective become typically:

$$T_{\text{vis}}^{V4} \simeq \frac{4 h_0^2}{3 a_0^2} \log \bar{R}_{\text{vis}} \sim \frac{4 h_0^2}{3 a_0^2} \quad (46)$$

$$T_{\text{eff}}^{V4} \simeq \frac{4 h_0^2}{3 a_0^2} \log \bar{R}_{\text{eff}} \sim \frac{8 h_0^2}{3 a_0^2} \quad (47)$$

The conditions for this regime to arise are the following:

$$C < \simeq \frac{4}{3} \frac{h_0^2}{a_0^2} \log \bar{R}_{\text{eff}} < 1 \quad (48)$$

$$\Sigma_c/2 < C \quad (49)$$

Equation (48) stipulates that the time at which cavitation is effective lies within stage *V4*, while Equation (49) is the condition for the cavitation threshold to be reached prior to stage *V4*, *i.e.*, during stage *V3*.

The second inequality in Equation (48) is always satisfied for thin samples. The other two inequalities can be satisfied only if:

$$\Sigma_c < \frac{8}{3} \frac{h_0^2}{a_0^2} \log \bar{R}_{\text{eff}} \quad (50)$$

$$\sigma_c < \frac{8}{3\pi} \frac{K h_0^3}{a_0^4} \log \bar{R}_{\text{eff}} \quad (51)$$

This is not the case in our series of experiments, since  $\sigma_c$  is necessarily greater than  $10^5$  Pa (see Section 2), while the right-hand side of (51) is on the order of  $3 \cdot 10^3$  Pa (with  $K \simeq 4 \cdot 10^5$  N/m,  $a_0 \simeq 5 \cdot 10^{-3}$  m and  $h_0 \simeq 10^{-4}$  m).

#### 5.4.7 Elastic cavitation

From the material point of view, the cavity growth implies a deformation mode (azimuthal stretching around the cavity) that is distinct from the usual traction (shear in Poiseuille deformation towards the centre). As a consequence, the resistance of the Maxwellian material to cavity growth depends on the growth rate.

In the regimes described above, the cavity growth rate  $\dot{R}/R$  is fastest when the cavity becomes effective. For cavitation developing from regime *V3*, it is on the order of  $2AT_{\text{eff}} \simeq 2\sqrt{A \log \bar{R}_{\text{eff}}}$ . From regime *V4*, it is  $3a_0^2/4h_0^2$ .

When  $\dot{R}/R < 1/\tau$ , the growth is liquid-like, as described above. When  $\dot{R}/R > 1/\tau$ , however, the growth should depend on the elastic properties of the material. If the stress then exceeds the elastic modulus, *i.e.*, Gent's threshold (1), the cavity should expand to macroscopic (effective) size. By contrast, if the stress is lower than the elastic modulus, then the growth rate should stabilize at a value that allows viscous growth:  $\dot{R}/R \sim 1/\tau$ .

In the present situation, the elastic modulus (see Section 3.2) is lower than the cavitation threshold (which is around atmospheric pressure). Hence, the cavity growth becomes elastic whenever the growth rate  $\dot{R}/R$  exceeds  $1/\tau$ .

#### 5.4.8 When delayed is too late

Cavitation from stage *V5*, called regime *R1358*, implies that cavitation is instantaneous since stage *V5* is very brief. In the present paragraph, we discuss whether viscously delayed cavity growth may hinder cavitation from this stage altogether.

The duration of regime *V5* is discussed in Appendix B.2 of Reference [9]. It is on the order of:

$$\sqrt{\frac{C}{2}} \frac{1}{2} \left( \frac{1}{2C} \right)^{2/5} = \frac{1}{4} (2C)^{1/10} \quad (52)$$

As for the maximum flow-induced tensile pressure component during stage *V5*, it was estimated as:

$$\mathcal{F}H|_{\text{max}} \simeq \frac{(T+1)^2}{4} \simeq \frac{C}{8} \quad (53)$$

Using Equation (29) combined with both above equations, one obtains that during stage  $V5$ , a cavity can grow by a factor equal to at most

$$\frac{R_{V_5^+}}{R_{V_5^-}} \leq e^{2A \frac{C}{8} \frac{1}{4}(2C)^{1/10}} \simeq e^{\frac{3}{128} \frac{a_0^2}{h_0^2} (2C)^{1/10}} \quad (54)$$

where  $R_{V_5^-}$  (resp.  $R_{V_5^+}$ ) is the cavity radius immediately before (resp. after) stage  $V5$ . For the typical values of the sample dimensions  $a_0 \simeq 5 \cdot 10^{-3}$  m and  $h_0 \simeq 10^{-4}$  m or  $h_0 \simeq 5 \cdot 10^{-5}$  m, one obtains:

$$\frac{R_{V_5^+}}{R_{V_5^-}} \leq \simeq e^{0.59 (2C)^{1/10}} \quad (h_0 \simeq 10^{-4} \text{ m}) \quad (55)$$

$$\frac{R_{V_5^+}}{R_{V_5^-}} \leq \simeq e^{2.3 (2C)^{1/10}} \quad (h_0 \simeq 5 \cdot 10^{-5} \text{ m}) \quad (56)$$

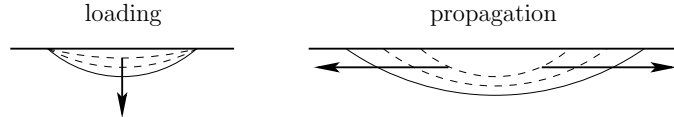


Figure 27: Crack loading and propagation at the interface between a rigid body and a deformable material. The behaviour of a purely elastic material is well-known. At low tensile stresses (loading), the existing crack keeps its original dimension and the situation is quasistatic. Once the threshold stress has been reached, propagation occurs and the crack broadens very rapidly. For a viscoelastic liquid such as a Maxwell fluid, however, the (slow) loading stage (which is enabled by the hysteresis of the contact angle or by anchoring of the triple line) is followed by a quasistatic propagation (dewetting) which — let aside propagation velocity — is very similar to crack. In this stage, depending on the dynamics of the applied tensile stress, the dewetted region may widen at an increasing rate. Then, when the dewetting rate becomes high, the crack may behave elastically until propagation is complete.

## 5.5 Crack triggering and propagation

The question of the triggering and propagation of crack should be considered very carefully in the present context.

Our material behaves roughly like a Maxwell fluid (see Section 3.2), and we have considered (see Figure 31) that cracks are triggered while the macroscopic deformation in the material is viscous ( $T \gg T$ ), at least in regimes  $R1379$  and  $R139$ .

The simple discussion of the crack threshold in paragraph 2.3, based on the assumption that the sample behaves elastically, must therefore be refined. This is particularly true for Griffith's criterion (8).

### 5.5.1 Elastic or viscous crack?

In the present experimental situation, the applied stress increases linearly with time (stage  $E1$ ,  $E2$  or  $V3$ ).

(i) At large loading rates, the material remains elastic until crack propagates, and Griffith's approach can be applied.

(ii) Conversely, at very low loading rates, the material behaves elastically only for a short period of time at early times. At all later times, it behaves as a liquid and may display dewetting.

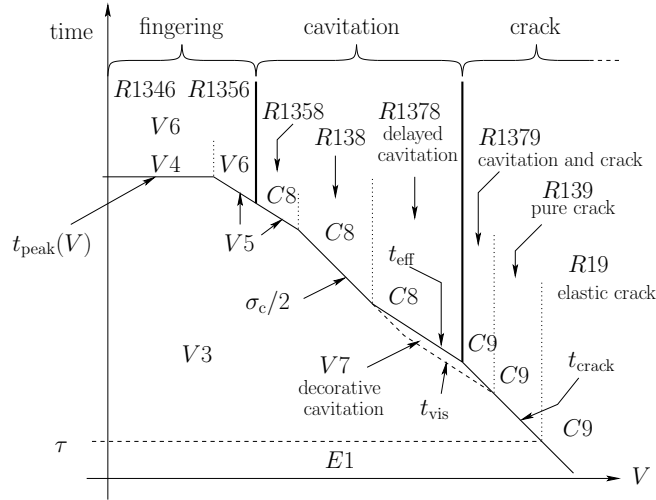


Figure 28: Expected force peak time as a function of the traction velocity. Stage  $V3$  (compliant machine and viscous sample) ends up with one of the following mechanisms: fingering, more rapid viscous flow ( $V5$ ), instantaneous cavitation ( $C8$ , time  $T_{\text{cav}}$ ), slow bubble growth ( $V7$  between both dotted lines that represent times  $T_{\text{growth}}$  and  $2T_{\text{growth}}$ ), or crack ( $C9$  at time  $T_{\text{crack}}$ ). Stage  $V7$  (slow bubble growth) can either continue up to the full bubble development (delayed cavitation), or be interrupted by crack propagation (the sample then displays both cavitation and crack).

At moderate velocities, dewetting may resemble disk-like cavitation in the vicinity of the surface as described briefly in [25].

(iii) At intermediate loading rates, as it acquires an increasing propagation rate, dewetting may progressively turn into elastic crack propagation. A detailed observation and analysis of such phenomena is given in Refs. [11, 26, 27].

### 5.5.2 Crack threshold in the present experimental situation

It appears from the above discussion that in order to determine how interfacial cracks may be triggered and how they may propagate in the present context, a more elaborate discussion should be carried out and include the dissipation around the crack tip in a viscoelastic sample as it propagates [11, 26, 27].

Such a detailed discussion goes beyond the scope of the present work. In the discussions below, we do not specify the expression of the threshold stress  $\sigma_{\text{crack}}$  for crack.

We are in a position, however, to provide some indications on the absolute magnitude of the effective crack threshold that should result from the considerations outlined above. Indeed, based on the observations of Section 4 and on the arguments of paragraph 5.3.2, it appears that interfacial cracks are triggered at a somewhat larger stress value than bulk cavities, and that the cavitation threshold is around atmospheric pressure. In other words, in terms of the (now obsolete) discussion on competing crack and cavitation in a *purely elastic, solid* material, the experiments reported here would correspond to a “moderately soft” material, *i.e.*, located between points A and B on figure 5.

## 5.6 Summary: complete phase diagramme for fingering, cavitation and crack

We are now in a position to predict the full system behaviour semi-quantitatively, and in particular the competition between cavitation and crack.

| Regime A / Regime B   | Condition in terms of $C_{\text{el}}$ and $T$   |
|---|---|
| Condition for Regime A  | Full, dimensional condition   |
| $R246/R1346$  | $C_{\text{el}} < 1$   |
| $C_{\text{el}} < 1$   | $\frac{3\pi}{2} G a_0^4 < K h_0^3$  |
| $R1346/R1356$   | $C_{\text{el}} T < 1$   |
| $C < 1$   | $\frac{3\pi}{2} \eta V a_0^4 < K h_0^3$   |
| $R1356/R1358$   | $C_{\text{el}} T < 4\Sigma_c$   |
| $C/8 < \Sigma_c/2$  | $\frac{3}{8} \eta V a_0^2 < p_{\text{atm}} h_0^3$   |
| $R1358/R138$  | $C_{\text{el}} T < \Sigma_c^2/2$  |
| $\sqrt{C/2} < \Sigma_c/2$   | $\sqrt{\frac{3}{\pi}} \sqrt{\eta V K} < p_{\text{atm}} h_0$   |
| $R138/R1378$  | $C_{\text{el}} T < \frac{3}{32} \frac{a_0^2}{h_0^2} \Sigma_c^2 / \log \bar{R}_{\text{eff}}$           |
| $\sqrt{\frac{1}{A} \log \bar{R}_{\text{eff}}} < \Sigma_c/2$           | $\frac{4\sqrt{\log \bar{R}_{\text{eff}}}}{\sqrt{\pi}} \sqrt{\eta V K} < p_{\text{atm}} a_0$           |
| $R1378/R1379$   | $C_{\text{el}} T < \frac{3}{32} \frac{a_0^2}{h_0^2} \Sigma_{\text{cr}}^2 / \log \bar{R}_{\text{eff}}$ |
| $\sqrt{\frac{1}{A} \log \bar{R}_{\text{eff}}} < \Sigma_{\text{cr}}/2$ | $\frac{4\sqrt{\log \bar{R}_{\text{eff}}}}{\sqrt{\pi}} \sqrt{\eta V K} < a_0 \sigma_{\text{crack}}$    |
| $R1379/R139$  | $C_{\text{el}} T < \frac{3}{32} \frac{a_0^2}{h_0^2} \Sigma_{\text{cr}}^2 / \log \bar{R}_{\text{vis}}$ |
| $\sqrt{\frac{1}{A} \log \bar{R}_{\text{vis}}} < \Sigma_{\text{cr}}/2$ | $\frac{4\sqrt{\log \bar{R}_{\text{vis}}}}{\sqrt{\pi}} \sqrt{\eta V K} < a_0 \sigma_{\text{crack}}$    |
| $R139/R19$  | $T < \Sigma_{\text{cr}}/2$  |
| $R1379/R19$   | $\sqrt{\frac{2}{\pi}} \sqrt{\eta V K} < a_0 \sqrt{G \sigma_{\text{crack}}}$                           |
| $T < \Sigma_{\text{cr}}/2$  |   |
| $R1378/R18$   | $T/C_{\text{el}} < \frac{8 \log \bar{R}_{\text{eff}}}{3} h_0^2/a_0^2$                                 |
| $T < \sqrt{\frac{1}{A} \log \bar{R}_{\text{eff}}}$                    | $\frac{1}{2\sqrt{\pi \log \bar{R}_{\text{eff}}}} \sqrt{\eta V K} h_0 < a_0^2 G$                       |
| $R138/R18$  | $T < \Sigma_c/2$  |
| $R1358/R18$   | $\sqrt{\frac{2}{\pi}} \sqrt{\eta V K} < a_0 \sqrt{p_{\text{atm}} G}$                                  |
| $T < \Sigma_c/2$  |   |
| $R13*/L.E.D.$   | $T/C_{\text{el}} < h_0/a_0$   |
| $T/C_{\text{el}} < h_0/a_0$   | $\sqrt{\frac{2}{3\pi}} \sqrt{\eta V K a_0 h_0} < G$   |
| $R246/L.E.D.$   | $T < h_0/a_0$   |
| $T < h_0/a_0$   | $\eta V a_0 < h_0^2 G$  |

Table 3: Equations that delineate the crossovers between the various regimes in phase diagramme 29.

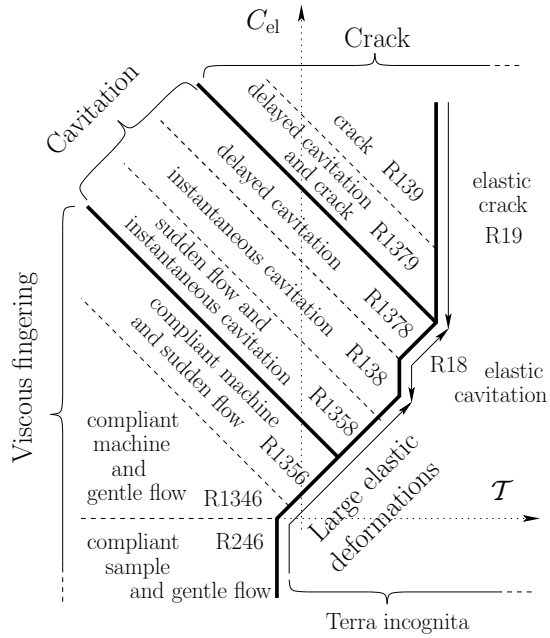


Figure 29: Phase diagramme of the system behaviour in terms of non-dimensional parameters  $C_{\text{el}}$  and  $\mathcal{T}$  (log-log plot). All three failure mechanisms (fingering, cavitation and crack) are included. The equations corresponding to all lines in the diagramme are to be found in Table 3 Varying the traction velocity as on Figure 28 amounts to visiting a horizontal line on the present diagramme (since  $\mathcal{T} \propto V$ ).

This competition is summarized on figure 28, which presents the time of the force peak as a function of the traction velocity in the case of fingering, cavitation or crack. More generally, the competition is illustrated as a phase diagramme on figure 29, in terms of non-dimensionnal parameters  $C_{\text{el}}$  and  $\mathcal{T}$ . Table 3 provides the equations for the crossovers between the various regimes in the phase diagramme

We now review each regime very briefly and provide the predicted time for the force peak.

### 5.6.1 Compliant sample and gentle flow: R246

In this regime, which is achieved for instance for a rather thick sample (low  $C_{\text{el}}$ ), the machine is more rigid than the sample. The sample therefore deforms and flows gently, almost exactly as prescribed by the motor. The sample eventually displays viscous fingering.

$$T_{\text{peak}} \simeq \mathcal{T} \quad \text{i.e.,} \quad t_{\text{peak}} \simeq \tau = \eta/G \quad (57)$$

### 5.6.2 Compliant machine and gentle flow: R1346

In this regime, as in most other ones below ( $C_{\text{el}} > 1$ ), the machine is more compliant than the sample: it deforms more than the sample at early times. Here, the sample flows gently, almost as prescribed by the motor, and displays viscous fingering. This regime was described earlier [9] as “regime 1”.

$$T_{\text{peak}} \simeq C \quad \text{i.e.,} \quad t_{\text{peak}} \simeq \frac{3\pi}{2} \frac{\eta a_0^4}{Kh_0^3} \quad (58)$$

### 5.6.3 Compliant machine and sudden flow: *R1356*

In this regime, the sample resists traction for so long that it eventually flows in a very sudden manner (stage *V5*), after which it flows gently with the motor and displays viscous fingering. This regime was described in [9] as “regime 2”.

$$T_{\text{peak}} \simeq \sqrt{\frac{C}{2}} \quad \text{i.e.,} \quad t_{\text{peak}} \simeq \sqrt{\frac{3\pi}{4} \frac{\eta a_0^4}{KVh_0^2}} \quad (59)$$

### 5.6.4 Sudden flow and cavitation: *R1358*

In this regime, the very sudden flow induces a strong (tensile) stress peak (see Figure 21) which triggers instantaneous cavitation. This regime was described in [9] as “regime 3”.

$$T_{\text{peak}} \simeq \sqrt{\frac{C}{2}} \quad \text{i.e.,} \quad t_{\text{peak}} \simeq \sqrt{\frac{3\pi}{4} \frac{\eta a_0^4}{KVh_0^2}} \quad (60)$$

### 5.6.5 Instantaneous cavitation: *R138*

In this regime, the cavitation threshold is reached while the gentle sample flow is still unsignificant, and the cavity growth is so rapid that it can be considered instantaneous.

$$T_{\text{peak}} \simeq \Sigma_c/2 \quad \text{i.e.,} \quad t_{\text{peak}} \simeq \frac{\pi}{2} \frac{p_{\text{atm}} a_0^2}{KV} \quad (61)$$

### 5.6.6 Delayed cavitation: *R1378*

In this regime, the cavity growth is delayed by viscous losses in the fluid.

$$T_{\text{peak}} \simeq \sqrt{\frac{1}{A} \log \bar{R}_{\text{eff}}} \quad \text{i.e.,} \quad t_{\text{peak}} \simeq \sqrt{4\pi \log \bar{R}_{\text{eff}}} \sqrt{\frac{\eta a_0^2}{KV}} \quad (62)$$

### 5.6.7 Decorative cavitation and crack: *R1379*

In this regime, the cavity growth is so much delayed that the tensile stress reaches the crack threshold and cracks propagate very rapidly. Meanwhile, however, the cavities have grown sufficiently to become visible, even though not enough to have any significant mechanical effect.

$$T_{\text{peak}} \simeq \Sigma_{\text{cr}}/2 \quad \text{i.e.,} \quad t_{\text{peak}} \simeq \frac{h_0}{2V} \sigma_{\text{crack}} \quad (63)$$

If the threshold stress  $\sigma_{\text{crack}}$  does not depend on the traction velocity  $V$ , then the peak time  $t_{\text{peak}}$  is proportional to  $1/V$ .

### 5.6.8 Crack: *R139*

In this regime, cracks develop before the cavities could become visible.

$$T_{\text{peak}} \simeq \Sigma_{\text{cr}}/2 \quad \text{i.e.,} \quad t_{\text{peak}} \simeq \frac{h_0}{2V} \sigma_{\text{crack}} \quad (64)$$

### 5.6.9 Elastic cavitation: *R18*

In this regime, cavitation develops while the sample is still deforming as an elastic body rather than as a viscous material. This regime is not described here: the cavity growth implies large stresses and large local deformations. Additional assumptions on the material behaviour would be needed, and this goes beyond the scope of the present work.

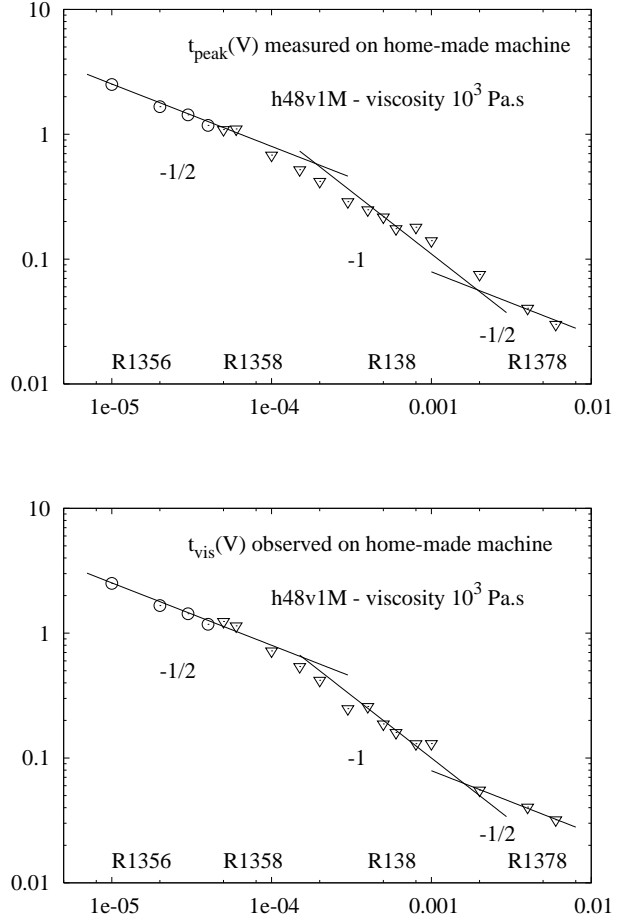


Figure 30: Time of the force peak (upper graph) and appearance time of failure mechanisms as observed with the home-made apparatus (lower graph) as a function of the traction velocity  $V$  (m/s). Circles indicate that viscous fingering was observed, and triangles correspond to cavitation. The sample used is the oil with viscosity  $\eta = 1000$  Pa.s. Power laws suggested by theory are indicated as guides for the eye.

#### 5.6.10 Elastic crack: $R19$

In this regime, cracks propagate while the sample is still elastic. Again, this regime is not described in the present work.

### 5.7 Test of the model against the experimental results

Let us now compare our experimental results (see paragraph 4.1 and our previous study [9]) with the theoretical power law predictions concerning the time of the force peak (see figure 28 and paragraph 5.6).

#### 5.7.1 Experiments on the 1 000 Pa.s oil

Figure 30 displays, among our previous results [9], those obtained for the 1000 Pa.s oil. For comparison, two quantities have been plotted as a function of the traction velocity  $V$  (m/s) for these measurements carried out with the home-made apparatus: the time of the force peak (upper

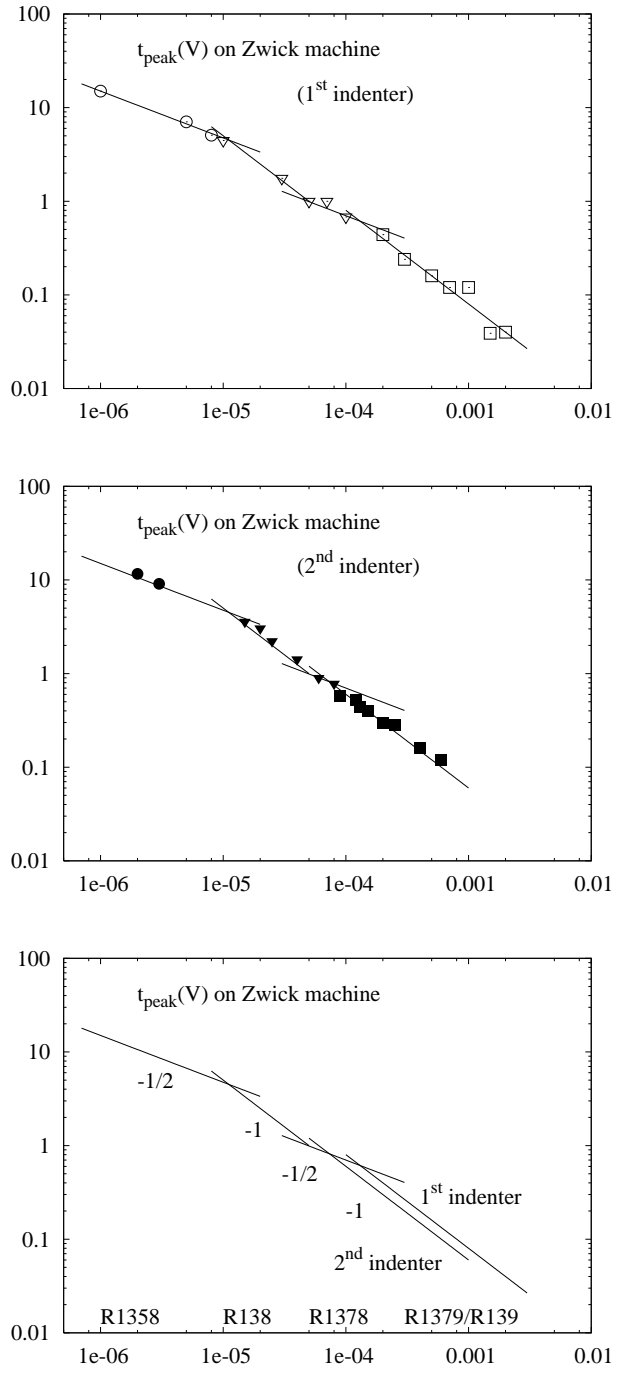


Figure 31: Time of the force peak as a function of the traction velocity on the commercial (Zwick) machine. The sample is the oil with  $\eta = 20000$  Pa.s. Two series of experiments are presented (upper graph with open symbols and middle graph with filled symbols), which were conducted with two, in principle identical, steel indenters. Observation of the indenter after the separation is complete and interpretation of the traction curves indicate that fingering (circles), cavitation (triangles) or crack (squares) has occurred. Power laws suggested by theory are indicated as guides for the eye. They are reported on the lower graph for comparison.

graph) and the appearance time of failure mechanisms (lower graph). Circles indicate that viscous fingering was observed, and triangles correspond to cavitation. The power laws suggested by theory for regimes  $R1356$  and  $R1358$  (sudden flow, slope  $-1/2$ ),  $R138$  (instantaneous cavitation, slope  $-1$ ) and  $R1378$  (delayed cavitation, slope  $-1/2$ ), are compatible with the data, although not fully convincing, on the upper graph. They are somewhat more convincing on the lower graph (observed appearance time for fingering or cavitation).

The final  $-1/2$  slope confirms the existence of delayed cavitation and refines the interpretations given in reference [9].

### 5.7.2 Experiments on the 20 000 Pa.s oil

The results obtained on the  $\eta = 20000$  Pa.s sample are presented on Figure 31. The time of the force peak measured on the commercial (Zwick) machine is plotted as a function of the traction velocity. Two series of experiments are presented. They were carried out with two, in principle identical, steel upper plates, which may differ slightly in — for instance — surface roughness. The symbol shapes indicate the failure mechanism that can be deduced from the observation of the indenter after the separation is complete and from the shape of the traction curve: fingering (circles), cavitation (triangles) or crack (squares). Crack corresponds to the absence of material on the indenter (adhesive failure). Cavitation corresponds to craters in the material that remains on the lower plate, or to the presence of a shouldering shape on the traction curve soon after the force peak. Fingering is revealed by visual observation of the material that remains on the plates.

Power laws suggested by theory for regimes  $R1358$  (sudden flow and cavitation, slope  $-1/2$ ),  $R138$  (instantaneous cavitation, slope  $-1$ ),  $R1378$  (delayed cavitation, slope  $-1/2$ ) and  $R1379$  or  $R139$  (crack, slope  $-1$ ) are indicated as guides for the eye. They fit the data rather convincingly.

The straight lines for each indenter (upper and middle graph of Figure 31) are reported on the lower graph for comparison. It appears that at moderate traction velocities, when fingering (circles) or cavitation (triangles) occurs, the force peak time does not seem to depend on the indenter surface. Indeed, all data follow quite accurately the same power laws with exponents  $-1/2$  and  $-1$ . Conversely, at higher traction velocities, the force peak times from each experiment are rather well described by a power law with the same exponent  $-1$  but with a different prefactor for each indenter.

This behaviour (same prefactor) was expected for viscous fingering, which is a *bulk* phenomenon. As for cavitation, the fact that it does not strongly depend on the properties of the interface between the sample and the indenter seems to indicate that it may nucleate in the bulk (although we cannot draw a definite conclusion on this matter with only two indenters tested).

Unsurprisingly, as an *interfacial* phenomenon, crack is readily affected by the indenter surface: the threshold for crack propagation is observed to be somewhat lower for the second indenter than for the first indenter.

In the case of the second indenter, the actual prefactors of the cavitation and crack regimes are very close to one another. As a result, the regime of delayed cavitation is not strikingly obvious. Only with the first indenter is it somewhat visible.

### 5.7.3 On the onset of cavitation

The reader may have noticed from Figure 31 that all data points on the low-velocity  $-1/2$  slope correspond to fingering: cavitation could not be inferred from the shape of the force curve in this regime; and direct visual observation was not possible for these series of experiments (conducted on the commercial machine).

In order to explain that no cavitation is present in the regime with a  $-1/2$  slope, let us recall the discussion on delayed cavitation arising during stage  $V5$  (see paragraph 5.4.8).

In Reference [9], for a  $5 \cdot 10^{-5}$  m sample, the transition between  $R1358$  and  $R138$  is observed for  $C \simeq 70$  and the transition between  $R1356$  and  $R1358$  is observed for  $C \simeq 1$ . The corresponding exponents in equation (54) are 3.8 and 0.63, respectively.

On Figure 31, the onset of regime  $R138$  (transition between slopes  $-1/2$  and  $-1$ ) is observed for  $V \simeq 1.2 \cdot 10^{-5} \text{ m/s}$ , *i.e.*, for  $C \simeq 1.6 \cdot 10^{-3}$ . As a result, the exponent in equation (54) is 0.33.

Hence, the cavity growth during stage  $V5$  in the experiments reported here is expected to be less pronounced than in the experiments reported in Ref. [9]. This may be partly explain why cavitation is not observed in the regime where stage  $V5$  is present (with slope  $-1/2$ ).

#### 5.7.4 On the orders of magnitude

As mentioned above, the expressions given in paragraph 5.6 account for the dependence of the peak time  $t_{\text{peak}}$  on velocity quite well (see Figure 31). They do not, however, account for the correct orders of magnitude when the material parameters are taken as  $G = 3 \cdot 10^3 \text{ Pa}$  and  $\eta = 20000 \text{ Pa.s}$ .

We believe that this discrepancy has its origin in the strongly non-Maxwellian character of the sample rheology (see Figures 6 and 7).

## 6 Conclusion and perspectives

We conducted probe-tack experiments on highly viscous silicon oils. Beyond viscous fingering and cavitation reported in a previous work [9], we observed delayed cavitation and interfacial fracture.

We constructed a theoretical model of how a Maxwell fluid should behave in such a probe-tack experiment, including considerations on crack thresholds and on cavitation thresholds and growth kinetics. Meanwhile, we showed that atmospheric pressure contributes to the traction force both in the case of cavitation [9, 10] and (in the present work) in the case of crack.

Although the rheology of the silicon oils we used departs from that of a Maxwell fluid substantially, we were able to give a possible explanation for the existence of the various regimes observed experimentally: cavitation alone, delayed cavitation, cavitation followed by crack, and pure crack.

Let us finally discuss two points.

1. Why did our approach work at all? Why did observe phenomena not unrelated with those observed in true adhesive materials?
2. What further rheological features should one include to mimic adhesive materials more closely?

### 6.1 Why did this approach work?

The above reported phenomena are very similar to those observed in adhesives. This may appear surprising, as the rheology of the systems we used (silicon oils) notably differs from that of adhesive materials. In particular, silicon oils are viscoelastic *liquids* while adhesive materials are viscoelastic *solids*.

In fact, this can be understood very simply by considering the possible rheological properties [28] of a soft material (figure 32). The distinction between solid and liquid appears only at long time scales: either the material develops a permanent resistance to flow (and it is a solid) or it eventually flows (it is then a liquid). At shorter time scales, only elastic and viscous characters are relevant.<sup>6</sup>

Now, our theoretical predictions deal with two different stages in the course of traction:

1. triggering the failure mechanisms; this happens while the material is still weakly deformed and still has not had time to display its solid or liquid character;
2. the force curve after cavitation has occurred; the material has then been strongly deformed to allow for the cavity growth; the *viscous* description we gave of this deformation (where *plastic* may have been more appropriate) is qualitatively valid.

---

<sup>6</sup>Indeed, beside the usual elastic solid and viscous liquid, soft materials include elastic liquids (generically represented by the Maxwell model) and viscous solids (generically represented by the Voigt or Kelvin model).

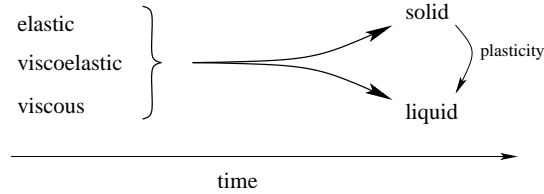


Figure 32: Rheology of soft materials under weak stress (schematic representation). On rather short time scales, depending on its molecular architecture (branching) and on frequency, the material may behave in a rather elastic or in a rather viscous manner. On long time scales, either it develops a permanent resistance to flow (and it is a *solid*), or it eventually flows (and it is a *liquid*). For some solid materials, a higher stress may trigger the flow (this is *plasticity*). Depending on the order of magnitude of the corresponding stress threshold, one usually refers to such a material either as a *yield stress fluid* or as a *plastic solid material*.

## 6.2 Extending the material rheology

The choice made in the present work to study a material with a Maxwellian behaviour (or more generally, any viscoelastic liquid material whose behaviour at large stresses is not specified) suffers some limitations.

- Some (large traction velocity) regimes of the macroscopic sample deformation are not accessible (see region “Terra incognita” on Figure 20).
- The large deformations around cavities can be adequately described in the slow, viscous regime but not in the faster, elastic regime.

In order to address these questions, the material should either have a narrow elastic regime at weak stress, followed by a plastic behaviour, or be able to sustain very large elastic deformations before it yields (or hardens).

True adhesive materials are often physically crosslinked and thus may display a plastic behaviour, at least at moderate stresses. (At higher stresses and deformation rates, broken physical crosslinks may not have time to reconnect and the material may become thinner and eventually break). Thus, extending the material rheology to viscoelastic plastic solids and to large elastic deformations will be important to capture more extensively the behaviour of true adhesive materials, essentially during three stages:

- at the early stages of traction under large traction velocities, when large shear stresses develop within the confined sample;
- once cavitation has been triggered, for the cavity development and growth kinetics;
- once cavitation has fully developed, when the cavity walls experience continued stretching and may induce interfacial cracks

## Acknowledgments

Differential equations were solved and plotted with softwares Scilab and Gnuplot. Drawings were made with Xfig. The corresponding scripts and original files are to be found at the end of the LaTeX source of the present article.

## A Confined Maxwell fluid under traction

In the present Appendix, we first compute the flow of a Maxwell fluid that is confined (thickness  $h$ , initial value  $h_0$ ) between two disks (radius  $a$ , initial value  $a_0$ ) when the disks are separating at

velocity  $\dot{h}$ . We then apply the result to the probe-tack situation where the motor is pulling on the plates at constant velocity  $V$  *via* the force sensor which behaves like a spring.

For later convenience, let us define the (constant) volume  $\Omega = \pi a_0^2 h_0 = \pi a^2 h$  of the sample. Let also  $r$  be the distance from the axis of symmetry, and  $z$  be the altitude perpendicularly to the plates, with  $z = 0$  at mid-height  $z = \pm h/2$  at the plates.

### A.1 Maxwell fluid in confined geometry

When the disks are pulled apart, the fluid is mainly sheared due to its strong confinement ( $h \ll a$ ). Provided some approximations are valid (discussed in paragraph A.5 below), the local constitutive equation for a Maxwell fluid can be written as

$$\dot{\varepsilon} = \frac{\dot{\sigma}}{G} + \frac{\sigma}{\eta} \quad (65)$$

where  $\sigma$  is the shear stress,  $\dot{\varepsilon}$  is the shear strain rate,  $G$  is the material shear modulus at high frequencies, and  $\eta$  is the viscosity.

### A.2 Velocity field

As mentioned above, confinement implies mainly radial velocity, in other words, the lubrication approximation is valid (except in the vicinity of the sample edges because of recirculation and in the very center where the radial velocity becomes smaller than the velocity along the vertical axis  $z$ ).

The magnitude of the radial velocity, averaged over the sample thickness, is fixed by volume conservation:

$$\int_{-h/2}^{+h/2} v(r, z) dz = v(r) = \frac{r}{2h} \dot{h} \quad (66)$$

The velocity profile along direction  $z$  reflects the balance between shear stress and pressure gradient *via* the constitutive equation of the fluid. Classically, for a Newtonian fluid, the profile is parabolic. In the present case, since equation (65) is linear and since convective effects are negligible (see paragraph A.5 below), the profile is still parabolic:

$$v(r, z) = v(r) \frac{3}{2} \left[ 1 - \frac{z^2}{(h/2)^2} \right] \quad (67)$$

### A.3 Pressure field and total force

The local stress balance  $\partial_r p = \partial_z \sigma$  (where  $\sigma$  is the  $rz$  component of the stress) implies that the pressure gradient is related to the shear stress on the plates:

$$\sigma|_{\text{plate}} = \frac{h}{2} \partial_r p \quad (68)$$

Taking the time derivative:

$$\dot{\sigma}|_{\text{plate}} = \frac{\dot{h}}{2} \partial_r p + \frac{h}{2} \partial_r \dot{p} \quad (69)$$

Also, from equation (67), the shear rate at the plate is given by

$$\dot{\varepsilon}|_{\text{plate}} = \frac{3\dot{h}}{h^2} r \quad (70)$$

Combining equations (65), (69), (69) and (70):

$$\frac{3\dot{h}}{h^2} r = \left[ \frac{\dot{h}}{2G} + \frac{h}{2\eta} \right] \partial_r p(r) + \frac{h}{2G} \partial_r \dot{p}(r) \quad (71)$$

Taking  $p(a) = p_{\text{atm}}$  and integrating from  $r$  to  $a$ , we obtain an equation for the pressure field:

$$\frac{3\dot{h}}{h^2} \frac{1}{2} (a^2 - r^2) = \left[ \frac{\dot{h}}{2G} + \frac{h}{2\eta} \right] [p_{\text{atm}} - p(r)] + \frac{h}{2G} [\dot{p}(a) - \dot{p}(r)] \quad (72)$$

where  $\dot{p}(a) = \dot{p}(r)|_{r=a} = -\dot{a} \partial_r p|_{r=a}$  can be neglected according to assumption (79). Integrating over the disk surface area and using  $F = \int_0^a [p_{\text{atm}} - p(r)] 2\pi r \, dr$ , we obtain the equation for the force:

$$\frac{3\dot{h}}{h^2} \frac{1}{2} \frac{\pi}{2} a^4 = \left[ \frac{\dot{h}}{2G} + \frac{h}{2\eta} \right] F + \frac{h}{2G} \dot{F} \quad (73)$$

Using  $\Omega = \pi a^2 h$  and  $\eta = G \tau$ :

$$\frac{3}{2\pi} \Omega^2 G \frac{\dot{h}}{h^5} = \dot{F} + \frac{F}{\tau} \left( 1 + \frac{\dot{h}}{h} \right) \quad (74)$$

#### A.4 Coupling with the machine and evolution equation

Using the spring equation

$$F = K(h_0 + Vt - h) \quad (75)$$

and the adimensional variables (Table 2), the differential equation (74) can be written as:

$$\left( \frac{C}{H^5} + \mathcal{T} \right) \dot{H} - \mathcal{T} = \mathcal{F} = 1 + T - H \quad (76)$$

The above equation, which is identical to Equation (22), describes the behaviour of a Maxwell-like system in a probe-tack geometry. We now discuss its validity.

#### A.5 Validity of the local equation

Equation (65), which we used to derive the force response of the sample (Equation 74), involves the sole shear component  $\sigma_{rz}$  of the stress. We shall now discuss whether or not it is valid to use this simple, scalar equation in the present context.

The relevant tensorial equation for a Maxwell fluid such as a polymer melt is the upper-convected Maxwell equation:

$$\dot{\sigma}^d + (v \cdot \nabla) \sigma^d - (\nabla v)^T \cdot \sigma^d - \sigma^d \cdot \nabla v = G \dot{\varepsilon} - \frac{\sigma^d}{\tau} \quad (77)$$

where  $\sigma^d$  is the deviatoric (*i.e.*, traceless) part of the stress:

$$\sigma^d = \sigma - \frac{I}{3} \text{tr}(\sigma) \quad (78)$$

The second term in Equation (65) is the usual gradient term in transport derivatives. The third and fourth terms, which involve the velocity gradient, and are one (*upper-convected*) form of the convective terms that are relevant when transporting a tensorial quantity that is linked to the underlying material medium.

The use of the simpler equation (65) instead of the full equation (77) implies that both following conditions be satisfied:

$$(v \cdot \nabla) \sigma^d \ll \dot{\sigma}^d \quad (79)$$

$$(\nabla v)^T \cdot \sigma^d + \sigma^d \cdot \nabla v \ll \dot{\sigma}^d \quad (80)$$

The components of these two tensor equations can be expressed as:

$$v_r \partial_r \sigma_{rr}^d \ll \dot{\sigma}_{rr}^d \quad (81)$$

$$v_r \partial_r \sigma_{rz}^d \ll \dot{\sigma}_{rz}^d \quad (82)$$

$$v_r \partial_r \sigma_{zz}^d \ll \dot{\sigma}_{zz}^d \quad (83)$$

$$2\sigma_{rr}^d \partial_r v_r + 2\sigma_{rz}^d \partial_z v_r \ll \dot{\sigma}_{rr}^d \quad (84)$$

$$\sigma_{rr}^d \partial_r v_z + \sigma_{zz}^d \partial_z v_r \ll \dot{\sigma}_{rz}^d \quad (85)$$

$$2\sigma_{zz}^d \partial_z v_z + 2\sigma_{rz}^d \partial_r v_z \ll \dot{\sigma}_{zz}^d \quad (86)$$

Because the entire calculation carried out here is based on the lubrication approximation, the normal stresses  $\sigma_{rr}$  and  $\sigma_{zz}$  cannot be distinguished from the hydrostatic pressure. As a result, the deviatoric normal stresses are zero:

$$\sigma_{rr}^d = 2\sigma_{zz}^d \simeq 0 \quad (87)$$

As a result, among the above six conditions (equations 81–86), only Equation (82) provides a useable constraint:<sup>7</sup>

$$\frac{a}{h} \dot{h} \cdot \frac{1}{a} \cdot \frac{h^{5/2} F}{\Omega^{3/2}} \ll \frac{d}{dt} \left( \frac{h^{5/2} F}{\Omega^{3/2}} \right) \quad (88)$$

i.e.,

$$\frac{\dot{h}}{h} \ll \frac{\dot{F}}{F} \quad \text{or} \quad \frac{\dot{H}}{H} \ll \frac{\dot{F}}{F} \quad (89)$$

From the material point of view, the stress must be weak enough for the recoverable deformation to be small:

$$\frac{\sigma_{rz}}{G} \ll 1 \quad \text{i.e.,} \quad \frac{h^{5/2} F}{\Omega^{3/2}} \ll G \quad (90)$$

i.e.,

$$\mathcal{F} H^{5/2} \ll C_{el} \frac{h_0}{a_0} \quad (91)$$

Note that at short times, when the sample is elastic, weak stress implies small deformations, defined by equation (25). In particular, it implies  $H \simeq 1$ . Condition (91) then reduces to:

$$\mathcal{F} \ll C_{el} \frac{h_0}{a_0} \quad (92)$$

Applying this criterion to equation (24), one recovers condition (26).

## B System evolution: stages and crossovers

Here are two tables that summarize the results of the discussion in section 5.2, concerning all stages that can be encountered during a probe-tack experiment on a Maxwell fluid:

- Table 4 provides the values of the main variables in all stages  $E1, E2, V3, V4, V5$  and  $V6$ .
- Table 5 indicates the equations for the various crossovers.

Table 4 describes only stages where the macroscopic sample deformation is involved. It does not describe other stages ( $V7, C8, C9$ ), where the sample deforms *locally* around cavities or cracks. It provides the tensile stress  $\mathcal{F}H$ , however, which is the relevant variable for triggering cavitation or crack (see paragraph 5.3.1).

<sup>7</sup>It is not excluded that other conditions provide stringent constraints when expressed beyond the framework of the lubrication approximation, but such a detailed hydrodynamic study is beyond the scope of the present work).

| Stage name | Validity                                 | Main variable values   |
|------------|--|--|
| E1         | $C_{\text{el}} \gg 1$                    | $\mathcal{F} \simeq T \frac{C_{\text{el}}}{1+C_{\text{el}}} \simeq T$                |
|            | $T \ll \mathcal{T}$                      | $H \simeq 1 + \frac{T}{1+C_{\text{el}}} \simeq 1 + \frac{T}{C_{\text{el}}}$          |
|            | $T \ll C_{\text{el}} h_0/a_0$            | $\mathcal{F} H \simeq T$   |
| E2         | $C_{\text{el}} \ll 1$                    | $\mathcal{F} \simeq T \frac{C_{\text{el}}}{1+C_{\text{el}}} \simeq T C_{\text{el}}$  |
|            | $T \ll \mathcal{T}$                      | $H \simeq 1 + \frac{T}{1+C_{\text{el}}} \simeq 1 + T$                                |
|            | $T \ll h_0/a_0$                          | $\mathcal{F} H \simeq T C_{\text{el}}$   |
| V3         | $C_{\text{el}} \gg 1$                    | $\mathcal{F} = T$  |
|            | $T \gg \mathcal{T}$                      | $H \simeq (1 - 2T^2/C)^{-1/4} \simeq 1 + \frac{T^2}{2C} \simeq 1$                    |
|            |  | $\mathcal{F} H = T$  |
| V4         | $C \ll T \ll 1$                          | $\mathcal{F} \simeq C$   |
|            | $T \gg \mathcal{T}$                      | $H = 1 + T - C \simeq 1 + T \simeq 1$  |
|            |  | $\mathcal{F} H \simeq C$   |
| V5         | $C_{\text{el}} \gg 1$                    | $\sqrt{\frac{C}{2}} > \mathcal{F} > \frac{4\sqrt{2}}{C^{3/2}}$                       |
|            | $T = \sqrt{\frac{C}{2}} \gg \mathcal{T}$ | $2 < H < \sqrt{\frac{C}{2}}$   |
|            | $C = C_{\text{el}} \mathcal{T} \gg 1$    | $\mathcal{F} H \simeq (\sqrt{\frac{C}{2}} - H)H$                                     |
| V6         | $T \gg \mathcal{T}$                      | $\mathcal{F} H = \sqrt{\frac{C}{2}} \rightarrow C/8 \rightarrow \frac{2\sqrt{2}}{C}$ |
|            |  | $\mathcal{F} \simeq \frac{C}{T^5}$   |
|            |  | $H \simeq T + 1 \simeq T$  |
|            |  | $\mathcal{F} H \simeq \frac{C}{T^4}$   |

Table 4: Values of the main system variables during stages  $E1$ ,  $E2$ ,  $V3$ ,  $V4$ ,  $V5$  and  $V6$ .

|                         |                          |  |
|-------------------------|--------------------------|--|
| $E1 \leftrightarrow E2$ | $C_{\text{el}} \simeq 1$ | machine and sample<br>compliance competition |
| $E1 \rightarrow V3$     | $T \simeq \mathcal{T}$   | Maxwell transition                           |
| $E2 \rightarrow V4$     |                          |  |
| $V3 \rightarrow V5$     | $H - 1 \simeq 1$         | flow acceleration, force peak                |
| $V3 \rightarrow V4$     | $\dot{H} \simeq 1$       | flow stabilization, force peak               |
| $V4 \rightarrow V6$     | $H - 1 \simeq 1$         | sample starts deconfining                    |
| $V5 \rightarrow V6$     | $H - 1 \simeq T$         | fast to slow flow transition                 |

Table 5: Stage transition criteria and interpretation.

## References

- [1] For a short review on stickiness, see C. Gay, L. Leibler, *Physics Today* **52**, (1999) 48.
- [2] C. Creton, P. Fabre, in *The mechanics of adhesion* edited by D.A. Dilliard and A.V. Pocius (Elsevier, Amsterdam, 2002) 535.
- [3] C. A. Dahlquist, Proc. Nottingham Conf. on Adhesion, 1966 Fundamental and Practice (MacLaren and Sons, Ltd. London).
- [4] C. A. Dahlquist, in *Treatise on Adhesion and Adhesives*, R. L. Patrick (ed.), Dekker, New York (1969), 2.
- [5] A. Zosel, *Colloid and Polymer Sci.* **263**, (1985) 541.
- [6] H. Lakrout, P. Sergot, C. Creton, *J. Adhesion* **69**, (1999) 307.
- [7] A. J. Crosby, K. R. Shull, H. Lakrout, C. Creton, *J. Appl. Phys.* **88**(5) (2000) 2956–2966.
- [8] On the level of scaling laws, the compared triggering of internal and external cracks [7] can be estimated as follows.  
Internal cracks are triggered according to Griffith's criterion (8), which can be rewritten as:  $K_I \simeq \sigma_{zz} \sqrt{b} \simeq \sqrt{\mathcal{W}G}$  where the left hand-side is the mode I stress intensity factor since normal load is much larger than shear stress in that region of the sample. The corresponding applied force is:  $F_{\text{int}} \simeq \frac{a_0^2}{\sqrt{b}} \sqrt{\mathcal{W}G}$ .  
Similarly, the threshold for external cracks corresponds to a mode II crack since normal stress vanishes at the edge, while shear stress is dominant:  $K_{\text{II}} \simeq \sigma_{rz} \sqrt{h_0} \simeq \sqrt{\mathcal{W}G}$ . The length scale  $h_0$  in the stress intensity factor here reflects the stress damping by the parallel, rigid boundaries. The corresponding applied force is:  $F_{\text{ext}} \simeq \frac{a_0^3}{\sqrt{h_0^3}} \sqrt{\mathcal{W}G}$ .  
The ratio between both values is  $F_{\text{int}}/F_{\text{ext}} \simeq \sqrt{\frac{h_0^3}{a_0^2 b}}$  and corresponds to the expression obtained by Crosby *et al.* [7] with more elaborate tools.
- [9] S. Poivet, F. Nallet, C. Gay, J. Teisseire, P. Fabre *Eur. Phys. J. E* **15**, (2004) 97.
- [10] S. Poivet, F. Nallet, C. Gay, P. Fabre, *Europhys. Lett.*, 62(2) (2003) 244–250.
- [11] T. Ondarçuhu, *J. Phys. II France* **7**, (1997) 1893–1916.
- [12] A. N. Gent, P. B. Lindley, *Proc. R. Soc. Lond. A* **249**, 195 (1958).
- [13] A. N. Gent, D. A. Tompkins, *J. Applied Phys.* **40**(6), 2520–2525 (1969).
- [14] P.-G. de Gennes, C. R. Acad. Sci. (Paris) **320**, 193–197 (1995).
- [15] E. Raphaël, P.-G. de Gennes, *J. Phys. Chem.* **96** 4002–4007 (1992).
- [16] A. A. Griffith, *Phil. Trans. R. Soc. London A* **221**, 163 (1920).
- [17] C. Gay, L. Leibler, *Phys. Rev. Lett.* **82**(5), (1999) 936–939.
- [18] W. P. Cox, E. H. Merz, *J. Polym. Sci.* **28**, 619 (1958)
- [19] B. A. Francis, R. G. Horn, *J. Appl. Phys.* 89:4167–4174 (2001).
- [20] D. Derk, A. Lindner, C. Creton, D. Bonn, *J. Appl. Phys.* **93**, (2003) 1557.
- [21] J.J. Bikerman, *J. Colloid Sci.* **2**, (1947) 163.

- [22] J. Dolhofer, A. Chiche, V. Muralidharan, C. Creton, C.Y. Hui, *Int. J. Solids Struct.* **41**, (2004) 6111.
- [23] A. Chiche, J. Dolhofer, C. Creton, *Eur. Phys. J. E* **17**, (2004) 389.
- [24] [http://en.wikipedia.org/wiki/Sonoluminescence#Fluid\\_Mechanics](http://en.wikipedia.org/wiki/Sonoluminescence#Fluid_Mechanics)
- [25] K. R. Shull, C. Creton, *J. Polym. Sci. B: Polymer Physics*, **42**, 4023-4043 (2004).
- [26] P.-G. de Gennes, *Langmuir* **12**, (1996) 4497–4500.
- [27] F. Saulnier, T. Ondarçuhu, A. Aradian, É. Raphaël, *J. Phys. II France* **7**, (1997) 1893–1916.
- [28] <http://en.wikipedia.org/wiki/Rheology>